Tunable properties and potential half-metallicity in $(Co_{2-x}Ti_x)FeGe$ Heusler alloys: An experimental and theoretical investigation

Shambhu KC,[1,2,*] R. Mahat,[1,2] S. Regmi,[1,2] A. Mukherjee,[3] P. Padhan,[4] R. Datta,[3] W. H. Butler,[1,2] A. Gupta,[1,5] and P. LeClair[1,2,†]

[1]*Center for Materials for Information Technology (MINT), University of Alabama, Tuscaloosa, Alabama 35487, USA*
[2]*Department of Physics and Astronomy, University of Alabama, Tuscaloosa, Alabama 35487, USA*
[3]*International Center for Materials Science, Chemistry and Physics of Materials Unit, Jawaharlal Nehru Center for Advanced Scientific Research, Bangalore-560064, India*
[4]*Department of Physics, Nanoscale Physics Laboratory, Indian Institute of Technology Madras, Chennai-600036, India*
[5]*Department of Chemistry and Biochemistry, The University of Alabama, Tuscaloosa, Alabama 35487, USA*

(Received 5 April 2019; revised manuscript received 20 August 2019; published 8 November 2019)

A $Co_{2-x}Ti_xFeGe$ ($0 \leqslant x \leqslant 1$) Heusler alloy series has been synthesized and investigated in steps of $x = 0.125$. While the parent Co_2FeGe composition was previously reported to exhibit multi-phase structures, the novel substitution of Ti for Co is successful in stabilizing single-phase microstructures for compositions from $x = 0.125$ to 0.625. The single-phase compositions crystallized in a face-centered cubic crystal structure. Soft-ferromagnetic behavior and a very high Curie temperature, as high as 881 K, is obtained for alloys with the lowest Ti concentration. Magnetic and electrical properties of these alloys suggest the possibility of half-metallic behavior in them. Both experimental findings and theoretical calculations support that the substitution of Ti atoms displaces Fe atoms towards vacated Co sites. The theoretical calculations also predict half-metallic character in the alloys after Ti substitution. The alloys are found to be unusually hard, with Vicker's hardness approaching 12 GPa for the most Ti-rich material.

DOI: 10.1103/PhysRevMaterials.3.114406

I. INTRODUCTION

Heusler alloys are a remarkable class of materials showing a wide varieties of properties such as half-metallicity [1], shape-memory [2], superconductivity [3], noncollinear magnetism [4], high-temperature ferri- and ferromagnetism [5], tunable topological insulator property [6], large magneto-optical effects [7], thermoelectric effects [8], and many more, rendering them an extremely fruitful subject of research. Half-metallic behavior is one of the most sought-after properties of Heusler alloys because of its potential impact on spintronic devices [9–11]. As far as half-metallic behavior in Heusler alloys is concerned, Co-based Heusler alloys are considered to be promising because they often have high Curie temperatures (T_c), both calculated [12,13] and experimentally observed [14,15].

Many candidate half-metals have been predicted and the corresponding high-spin polarization has been measured at low temperature using tunneling magnetoresistance (TMR) [16] and giant magnetoresistance(GMR) [17]. However, the TMR and GMR values decrease significantly at room temperature [16,17], so it remains a challenge to find half-metallic material with large magnetoresistance values at room temperature for use in practical devices. Two main causes for the decrease of magnetoresistance at finite temperature are usually noted: the interface of the half-metallic ferromagnetic layer with a nonmagnetic layer in magnetic tunnel junctions (MTJ) may destroy the local half-metallic properties or result in reduced local exchange interactions, and the loss of bulk half-metallic behavior at finite temperature [5]. The interfacial issue can be in many cases mitigated by optimizing the growth conditions, choosing a nonmagnetic layer with a compatible electronic structure, and by minimizing the lattice mismatch between the ferromagnetic electrode and the barrier layer. The latter issue is related to the property of the ferromagnetic material itself and can be addressed by making the half-metallic behavior more robust. A method of doing this is to tune the Fermi level to the middle of the energy gap in one of the spin channels by substitution of one of the elements. Tremendous efforts have been made to search for robust half metals in substituted alloys and, several substitutional quaternary alloys have been discovered with improved spin polarization at room temperature [18–20].

While searching for a possible candidate alloy in order to tune half-metallic behavior by means of substitution, we found Co_2FeGe to be a promising candidate. Previously, ternary Co_2FeGe was reported theoretically to be a stable compound crystallizing in the $L2_1$ structure, but with no half-metallic behavior due to the Fermi level falling within the lower part of the minority conduction band [21]. Experimentally, Co_2FeGe was observed to show a multiphase bulk microstructure [21], suggesting that substitution might be necessary to stabilize a single-phase $L2_1$ material and tune the system toward half-metallicity. Varaprasad *et al.* [19]

*skc@crimson.ua.edu
†pleclair@ua.edu

were able to tune some useful properties in Co_2FeGe by substitution of Ga for Ge as $Co_2Fe(Ga_{1-x}Ge_x)$ alloy series and obtained spin polarization (P) up to 0.69. However, this value of P is still less than expected for ideal half-metals. Venkateswarlu *et al.* [22] studied a slightly different substitutional series $Co_2(Ti_{1-x}Fe_x)Ge$ experimentally, but did not find any signs of half-metallic behavior.

While the previous attempts of substitution were not completely successful, they motivated us to think about different approaches to substitution in this system. Substitution is generally made either for Y site (low valent transition metal) or Z site (main group element) of the parent X_2YZ alloy [20] and to the best of our knowledge, there are only a few reports on the substitution of X site (high-valent transition metal) in case of Co-based full Heuslers [23,24]. The structural change i.e., from $L2_1$ (X_2YZ, space group $Fm\bar{3}m$, No. 225) to Y ($XX'YZ$, space group $F\bar{4}3m$, No. 216) structure could be one possible argument why X site substitution was overlooked in past, as it makes identification of the exact structural order after substitution more challenging, especially in the intermediate substitution range. Thus a careful analysis of how the structural order changes while substituting "on the X site" with the goal of shifting the Fermi level towards the band-gap are the primary purposes of this work.

In the case when the Fermi level falls at the edge of the spin-down gap, Galanakis *et al.* [25] suggest that an expansion of the lattice should shift the Fermi level deeper in energy whereas the contraction should shift it higher in energy. In light of this, an expansion of the lattice should restore half-metallicity in the case of Co_2FeGe in which the Fermi level falls on the lower part of the minority conduction band. Ti, which has larger atomic radii than Co [26] should expand the lattice when substituted for Co. Hence, for the material in this study, Ti is substituted for Co in the parent Co_2FeGe alloy. An additional attempt was also made to substitute for Co with Fe, i.e., a $(Co_{2-x}Fe_x)TiGe$ alloy series. However, the compositions investigated ($x = 0.5, 0.75$) showed multiphase microstructures. Hence, in this paper, the synthesis and characterization of a bulk $(Co_{2-x}Ti_x)FeGe$ alloy series is reported, with a focus on structural stability and magnetic, electrical, and mechanical properties. Finally, a comparison of experimental findings is made with the theoretical calculations of electronic structure performed by using density functional theory (DFT).

II. EXPERIMENTAL APPROACH

A. Sample preparation and characterization techniques

Polycrystalline ingots of $(Co_{2-x}Ti_x)FeGe$ samples, with x varying in the steps of 0.125, were prepared by arc melting of the constituent elements (99.9 % pure, Alfa Aesar) in an argon atmosphere at a base pressure of 0.02 Pa. After each melting, the sample was flipped and remelted at least six times to enhance the homogeneity of mixing. An energy dispersive x-ray spectroscopy (EDS) detector equipped in a JEOL 7000 field emission scanning electron microscope (SEM) was used to ensure the target stoichiometry after the arc melting. To enhance further homogenization and facilitate the crystal growth, arc-melted pieces were sealed in evacuated quartz tubes and annealed. To make the comparison uniform across all compositions, only the samples which went through similar heat treatments (i.e., 950 °C for 3 days) are chosen for this work.

The heat treatments were followed by metallography [27] to produce a metallic shiny surface for microstructure analysis by optical and electron microscopes. After the heat treatment and metallography, the composition and homogeneity of the samples were again confirmed by using EDS. A Bruker D8 Discover x-ray diffractometer equipped with monochromatic Co-K_α ($\lambda = 0.179$ nm) radiation was used to obtain the x-ray diffraction (XRD) patterns to determine crystal structures. In order to minimize the influence of texturing in the observed intensities of XRD patterns, the samples were rotated in the phi (ϕ) direction while collecting the pattern. To fit the experimental pattern, simulated XRD patterns were generated by using commercial CARINE crystallographic 3.1 software [28] as well as custom in-house software [29], and Rietveld refinement was carried out using a MATCH! software based on the FULLPROF algorithm [30]. Electron backscatter detection (EBSD) in the JEOL 7000 SEM was used to further corroborate the structure observed in the XRD pattern.

Transmission electron microscopy (TEM) imaging and recording of electron diffraction (ED) patterns were performed in an aberration-corrected FEI TITAN (80–300 kV) microscope. High-resolution TEM (HRTEM) imaging was recorded under the negative spherical aberration coefficient (Cs) imaging condition with Cs ≈ -35 μm and defocus of $\approx$8 nm, which gives bright atom contrast and helps in direct interpretation of the structure [31]. The electron transparent samples were prepared first by mechanical thinning to a thickness of $\approx$20 μm and then Ar ion milling in Gatan PIPS to generate large electron transparent thin areas.

The low-temperature magnetic and electrical transport properties were studied in Quantum Design Physical Properties Measurement System (PPMS), while the high-temperature magnetization was measured using the Lakeshore VSM 7410. The mechanical properties were studied in terms of Vicker's hardness by using a Buehler model 1600-6100 microhardness tester.

B. Result and discussion

1. Microstructure analysis

Obtaining a phase-pure material so that the intrinsic properties of the substituted alloys can be determined is one of the primary goals of this work. Particularly for assessing magnetic properties, even a small percentage of an impurity phase will render any conclusions questionable at best. X-ray diffraction will not easily identify impurity phases if they are only a few percents of the overall volume. Microscopy is the most direct method of visualizing the surface morphology and identifying possible impurity phases, and this was the starting point of each investigation. Observing that there are areas with different contrast in optical microscopy can suggest the presence of impurity phases, and SEM with EDS allows one to directly measure whether areas of different contrast represent impurity phases or merely different crystallite orientations.

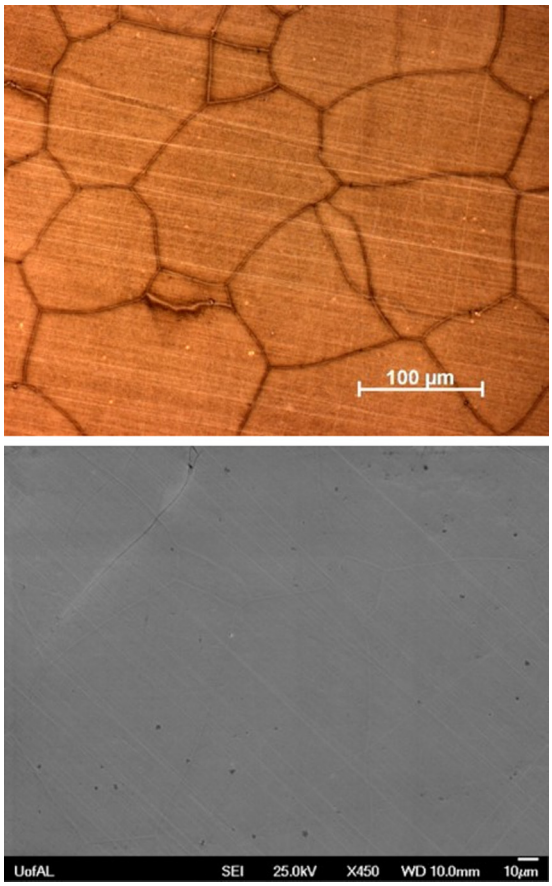

FIG. 1. (Top) Optical and (bottom) electron micrograph of $Co_{1.5}Ti_{0.5}FeGe$ heat treated at 900 °C for 3 days. Uniform granular structure can be seen with no other phases.

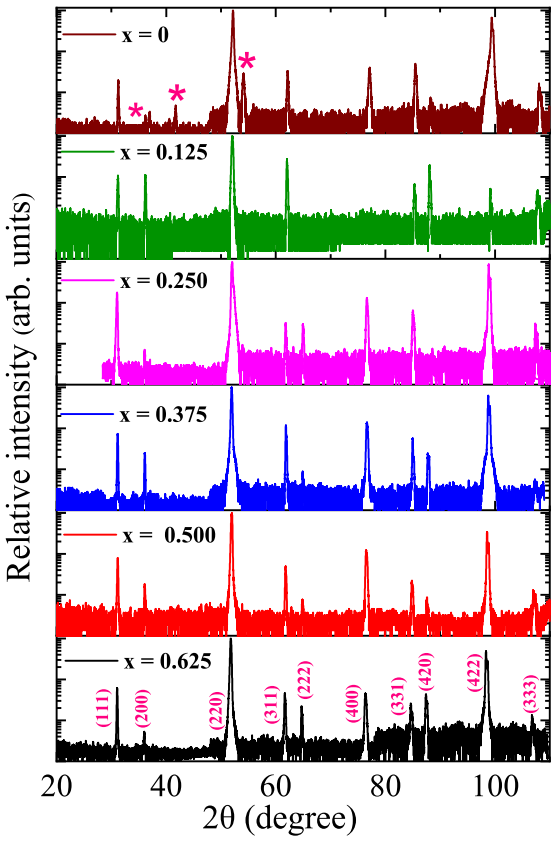

FIG. 2. The XRD patterns of $Co_{2-x}Ti_xFeGe$ alloy series heat-treated at 950 °C for 3 days collected using Co-K_α x-ray source.

For all samples, a detailed surface analysis was performed after careful grinding and polishing of the samples.

Multiphase behavior was clearly visible in the parent Co_2FeGe compound, in accordance with previous reports [21]. However, with the substitution of Ti for Co, the secondary phase began to disappear and uniform single-phase behavior was observed in the composition range ($x =$ 0.125–0.625). For the single-phase samples with less Ti ($x =$ 0.125 to ≈0.250), a slightly different composition was observed in the grain boundaries. On the other hand, samples with high concentrations of Ti ($x = 0.625$) showed evidence of secondary phases (though less than 1 %). For this reason, we considered the samples with intermediate compositions ($x = 0.375$–0.500) to be higher quality and focused more effort on their characterization and understanding. More detailed information on the evolution of single-phase behavior and microstructure images of the samples are provided in Ref. [27]. Figure 1 shows one such single-phase microstructure obtained for $x = 0.500$ with both optical and electron microscope images. Within the grains, for all the single-phase samples the stoichiometry measured by EDS was consistent with the target composition within an (instrumental) uncertainty of ≈5%. In the case of Co_2FeGe ($x = 0$), however, the composition was measured to differ from the target composition by more than 5%.

2. *Structure determination and atomic order analysis*

In the experimental XRD pattern, shown in Fig. 2, for Co_2FeGe ($x = 0$), peaks from impurity phases are visible and are marked with asterisks. The existence of impurity phases is consistent with the literature reports and our observation of multiphase morphology in the metallography images. However, for the Ti substituted samples, the impurity peaks were not visible, suggesting single-phase behavior consistent with our microscopy results. In the XRD patterns, for all single-phase samples, only three types of reflection peaks were observed; fundamental peaks with $h + k + l = 4n$ (220, 400, etc.), even superlattice peaks with $h + k + l = 4n + 2$ (200, 222, etc.) and odd superlattice peaks with $h + k + l = 2n + 1$ (111, 311, etc.). The presence of low-angle superlattice peaks is an indication of $L2_1$ type ordering in the alloys. Further, there were no peaks indexed with mixed odd/even indices (i.e., h, k, l are either all odd or all even). These facts indicate that the alloys are crystallized in a face-centered cubic structure.

It is challenging to determine the precise, detailed, atomic order in our alloys series. The crystal structure of a full Heusler alloy can be described using a 16 atoms unit cell, where there are four sites; 4a (0, 0, 0), 4b (0.5, 0.5, 0.5), 4c (0.25, 0.25, 0.25), and 4d (0.75, 0.75, 0.75) to be occupied. These four sites can be partitioned into two sublattices. One sublattice (A) consists of 4a and 4b sites, while the other (B) consists of 4c and 4d sites. If two of these sites (say 4a and 4b) of the same sublattice (A) are filled by the same atom,

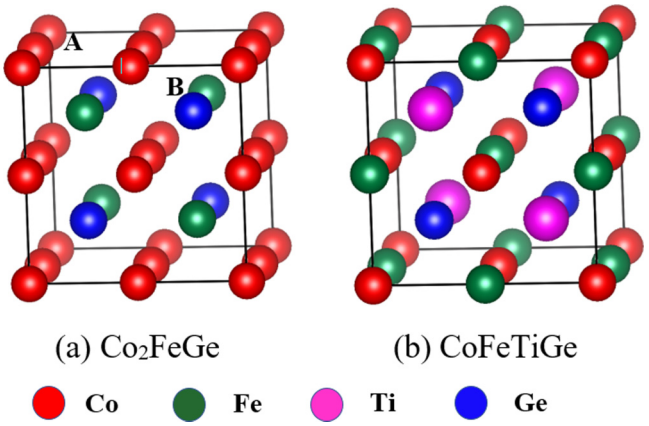

FIG. 3. Schematic representation of unit cell of a full Heusler (a) Co_2FeGe alloy assuming $L2_1$ structure (b) CoFeTiGe alloy assuming Y structure. Here, A and B refer to two sublattices.

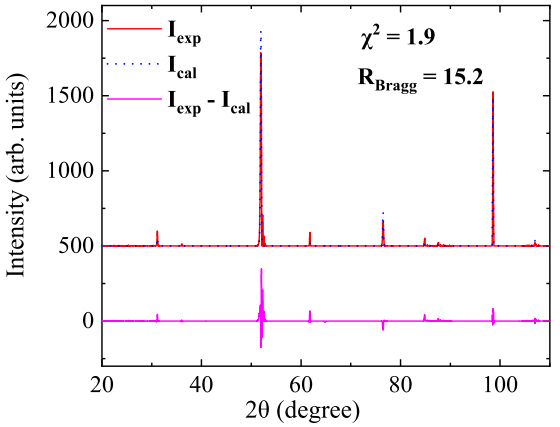

FIG. 4. Rietveld refinement performed on $Co_{1.5}Ti_{0.5}FeGe$ assuming first atomic configuration given in Table I. A good refinement was achieved with slightly higher fitness parameters attributed to sample texture and large grains size.

i.e., forming an octahedron surrounding the sites (4c and 4d) in another sublattice (B), then the structure is known as $L2_1$ (Space group $Fm\bar{3}m$, No. 225) structure, generally written as X_2YZ. However, if all four sites are occupied by four different atoms, the structure is called Y (Space group $F\bar{4}3m$, No. 216) structure and written as XX'YZ. In this structure, all the sites have tetrahedral symmetry. The parent alloy in the present case i.e., Co_2FeGe ($x = 0$) has been reported to have $L2_1$ structure with Co atoms occupying 4a and 4b sites, whereas Fe and Ge atoms on the 4c and 4d sites respectively as shown in Fig. 3(a) [19,21]. The other end member, i.e., CoFeTiGe has four different atoms [see Fig. 3(b)] and DFT calculations indicate that Y structure with Co, Fe, Ti, and Ge atoms occupying 4a, 4b, 4c, and 4d sites, respectively, is more stable than other occupations of Y lattice in such case [32,33].

In the light of this, it can be seen that there is a change in structural order from $L2_1$ ($x = 0$) to Y ($x = 1$) after Ti substitution. One can also notice that Fe atoms occupy two different sites; the 4c sites sharing the same sublattice with Ge when $x = 0$ and the 4b sites sharing the Co sublattice when $x = 1$. This is consistent with the general rules, which predict that atoms sharing the same sublattice with the main group element (Ge in the present case) should have the highest difference in their electronegativity due to the ionic nature of their bonding [5]. This makes Ti more likely to share the same sublattice with Ge than Fe or Co. Hence, we presume that Ti substitution will displace the Fe atoms towards vacated Co sites and it will fill the site previously occupied by Fe sharing the sublattice with Ge. We would like to stress here that this is just a presumed structure and we do not want to rule out the possibility of other types of chemical order at this stage. More detail about possible alternative chemical orders will be provided in Sec. III.

XRD is a useful tool to identify the exact chemical order in the crystals, however, if the participating atoms have similar x-ray scattering factors (as in the present case), it becomes difficult to distinguish the difference between possible structures in which atoms with similar scattering factors have been interchanged. The unknown degree of texturing in the samples further adds to the complexity as it alters the relative intensities of the peaks. Therefore, by relying only on the experimental XRD, we are unable to determine the precise chemical order (see Ref. [27] for details).

Nonetheless, in an attempt to push the XRD based structure analysis as far as possible, we performed Rietveld refinement for $Co_{1.5}Ti_{0.5}FeGe$ ($x = 0.500$). The refinement yielded a reasonably good fit for all of the structures, but the best fit was obtained for a structure that placed Co and Fe on the A sublattice and Fe, Ti, and Ge on the B sublattice. This fit is shown in Fig. 4 and the goodness of fit parameters are shown in Table I.

The Rietveld fit parameters reported above are slightly higher than those expected for a perfect fit, this can be attributed to the sample texture altering the relative intensities of the peaks compared to the calculated pattern. This is one of the reasons why the different configurations produced nearly the same fit parameters. In order to study the degree of texturing, phase purity, and to shed more light on the crystal structure, an EBSD inverse pole figure (IPF) map and phase map was performed on a relatively large area ($600\,\mu m \times 600\,\mu m$) of a $Co_{1.5}Ti_{0.5}FeGe$ sample. In the IPF [Fig. 5(a)], large grains with preferred orientations were seen, resulting in higher than expected intensity for some orientations, which could explain the relatively high values of the Rietveld fitting parameters. Similarly, in the EBSD phase map [Fig. 5(b)], more than 99%

TABLE I. Rietveld refinement goodness of fit parameters for some possible atomic configurations of $Co_{1.5}Ti_{0.5}FeGe$ ($x = 0.500$). These configurations will be described in detail in Sec. III.

Configuration	χ^2	R_{Bragg}
Co_6Fe_2-$Fe_2Ti_2Ge_4$	1.9	15.2
Co_5Fe_3-$CoFeTi_2Ge_4$	2.6	15.1
Co_6FeTi-Fe_3TiGe_4	2.7	16.1
Co_4Fe_4-$Co_2Ti_2Ge_4$	2.6	14.8
$Co_4Fe_2Ti_2$-$Co_2Fe_2Ge_4$	2.7	16.6
$Co_2Fe_4Ti_2$-Co_4Ge_4	2.6	15.5
Co_6Ti_2-Fe_4Ge_4	2.8	17.5
Co_5FeTi_2-$CoFe_3Ge_4$	2.2	20.0

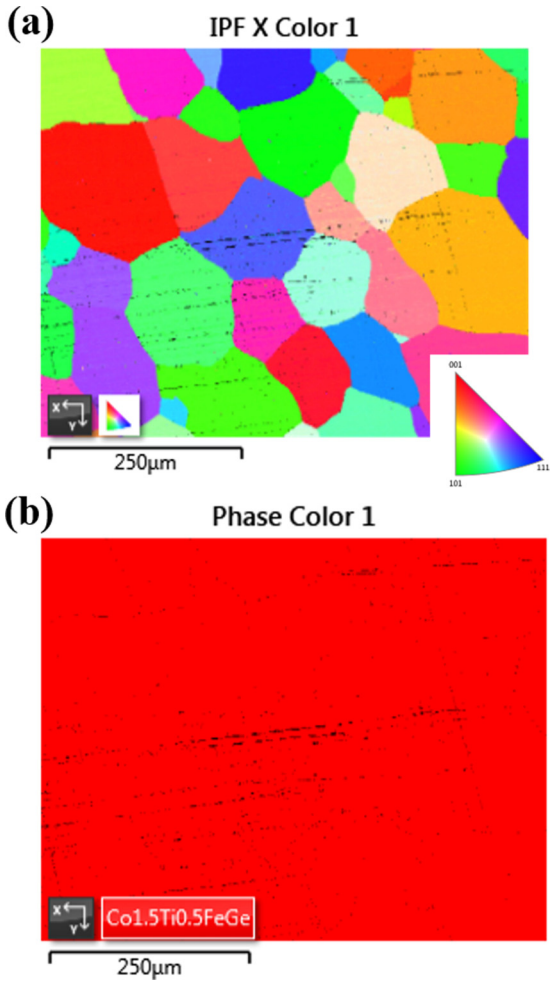

FIG. 5. (a) Inverse pole figure (IPF) color map of $Co_{1.5}Ti_{0.5}FeGe$ taken using EBSD in SEM showing grain orientation with respect to sample x direction. Large grains with some preferred texture can be observed. (b) The corresponding EBSD phase map of the same area showing single-phase behavior.

of the entire microstructure was observed to be consistent with the presumed structure (red-colored regions), with some zero solution regions (black spots) due to pores and polishing artifacts. All of the above provide plausible evidence for the presumed structure in which the substituted Ti atom displaces the Fe atom towards the vacated Co site as the crystal structure of our alloys.

Cohen's method with a Nelson-Riley error function [34,35] was then utilized to extract a precise lattice parameter from the experimental XRD data. The extracted lattice parameter was observed to increase linearly with Ti concentration (Fig. 6). This increase of lattice parameter is in agreement with Vegard's law [36] and can be explained in terms of the larger atomic radii of Ti (176 pm) [26] compared to that of Co (152 pm) [26]. Since practical device applications require thin films, any newly synthesized material should have comparable lattice mismatch with commonly used substrates in order to grow high-quality films. An experimental lattice parameter of 5.782 ± 0.002 Å was obtained for $Co_{1.5}Ti_{0.5}FeGe$. This lattice parameter offers a favorable lattice match with some

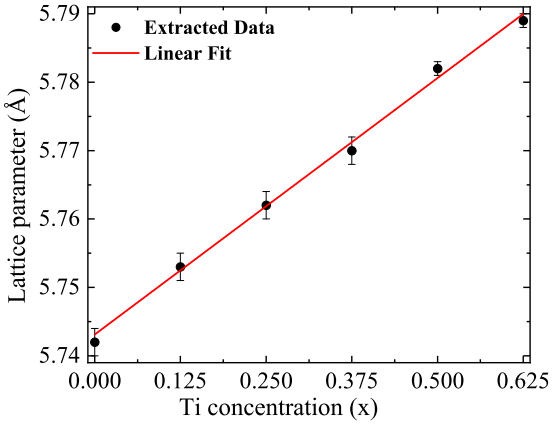

FIG. 6. Variation of extracted lattice parameter with Ti concentration, showing linear behavior.

of the most widely used substrates, in addition to being tunable by varying Ti content, making it feasible to grow high-quality epitaxial films. For instance, a lattice mismatch of 0.8% with Al_2O_3 (110) can be expected for $Co_{1.5}Ti_{0.5}FeGe$ (110). Similarly, a mismatch of 2.95% with MgO (100) with 45° rotation is expected for $Co_{1.5}Ti_{0.5}FeGe$ (100), and in fact this mismatch is smaller compared to other predicted Heusler half-metals (e.g., $Co_2FeAl_{0.5}Si_{0.5}$, $Co_2Cr_{0.6}Fe_{0.4}Al$, Co_2FeSi, etc.) [37,38].

HRTEM analysis was also performed on the $Co_{1.5}Ti_{0.5}FeGe$ sample. Both low-magnification TEM bright field and HRTEM images confirmed the formation of a single homogeneous phase. Bright-field and HRTEM images with corresponding diffraction pattern taken along ⟨111⟩ zone axis and its fast Fourier transform (FFT) are given in Fig. 7. The TEM patterns taken along other zone axes are included in Ref. [27]. No additional spots due to secondary phases could be observed. The interplanar spacing was measured for different planes with different zone axes, all of which gave nearly the same value of lattice parameter (a = 5.74 Å) and agreed quite well with the lattice parameter extracted from x-ray diffraction. No dislocations or other kinds of defects were observed in the TEM images.

3. *Magnetic characterization*

The temperature-dependent magnetization measurement of a series of heat-treated $Co_{2-x}Ti_xFeGe$ alloy with different x is shown in Fig. 8(a). The magnetization was measured with a 1000 Oe magnetic field in the temperature range of 300 to 1000 K. These alloys show paramagnetic ordering at 1000 K, and on cooling below 1000 K, the magnetic moments order ferromagnetically at Curie temperature (T_c). The T_c of these alloys is significantly above room temperature, and decreases with increasing x from $x = 0.125$ to 0.625. We also studied the field dependence of the magnetization $M(H)$ measured at 5 K [see Fig. 8(b)] and 300 K (see Ref. [27]). These $M(H)$ curves indicate the presence of soft-ferromagnetic ordering and the absence of a hysteresis loop at low field. The saturation magnetization (M_s) was extracted from an Arrot plot, i.e., by extrapolating the linear part of M^2 versus to H/M to $H/M = 0$ [see inset to Fig. 8(b)].

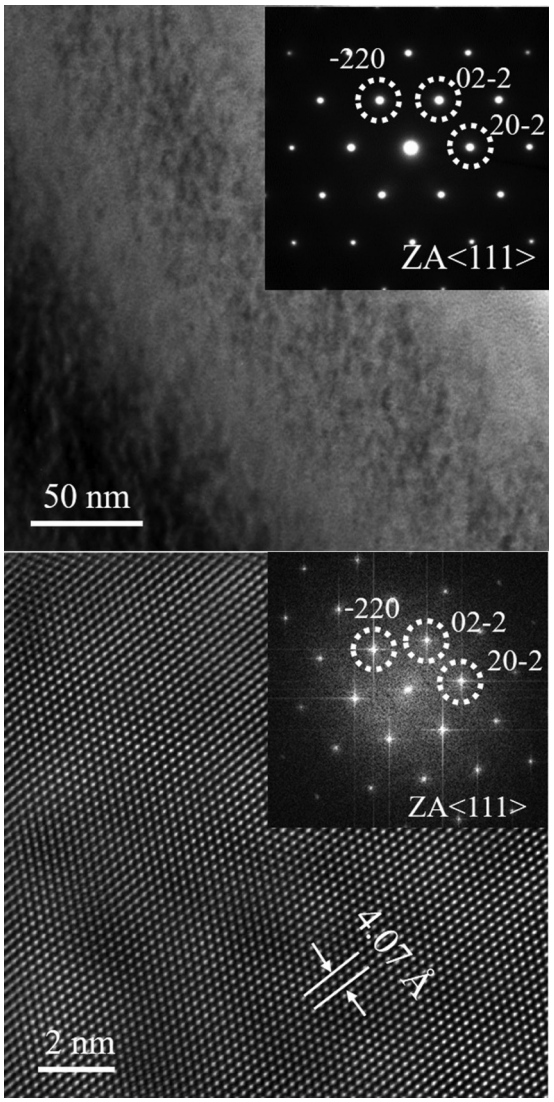

FIG. 7. (Top) TEM bright field image showing formation of homogeneous single phase, inset is the ED pattern along ⟨111⟩ zone axis. (bottom) Corresponding HRTEM image and FFT pattern (inset) confirming the single phase of the alloy.

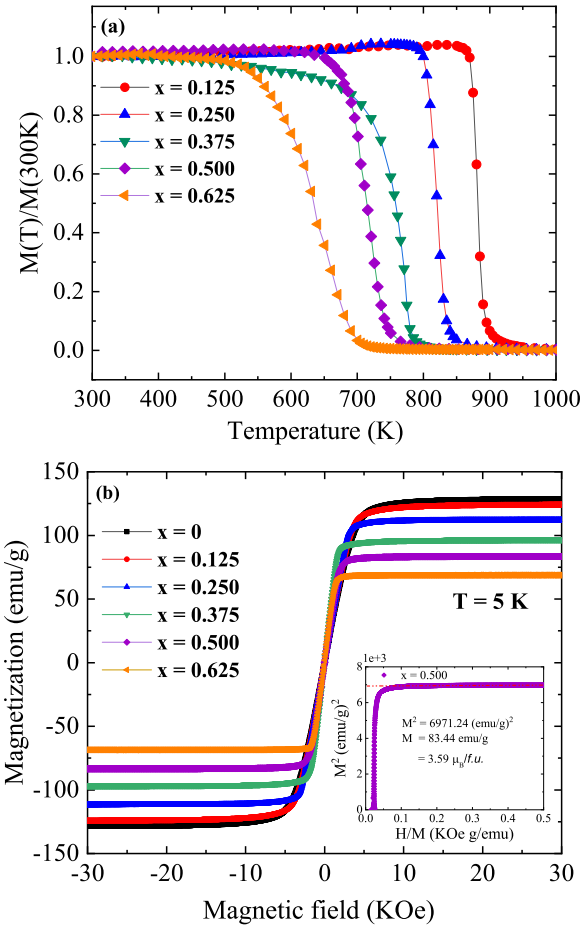

FIG. 8. (a) Temperature-dependent and (b) field-dependent magnetization curves for samples $x \leqslant 0.625$.

The M_s determined from M(H) varies linearly with the number of valence electrons of the alloys, see Fig. 9(a). The deviation from linear behavior at $x = 0$ is consistent with the presence of secondary phases as observed in XRD (see Fig 2) and microscopy (see Ref. [27]). The M_s values of these alloys at 5 K are close to the theoretical moment expected from the Slater-Pauling rule, as shown in Fig. 9(a). The quantitative agreement between the experimental and Slater-Pauling M_s is an indication that these alloys may be half-metals. The linear relation between T_c and M_s [see Fig. 9(b)] is because both M_s and T_c show a linear dependence on the number of valence electrons, as was reported for Co_2-based Heuslers [13] in the case where one of the sublattices (say A) is completely filled by Co atoms. Srinivas *et al.* [23] studied the magnetic properties of a $Co_{2-x}Fe_{1+x}Si$ alloys series, where the atomic fraction of Co was also less than 2. However, the extracted low-temperature saturation magnetic moments did not seem to follow the Slater-Pauling behavior in their case. Here, the system follows the Slater-Pauling behavior when the atomic fraction of Co is less than 2, adding one more degree of freedom to make substitutions and tune magnetic properties. The extracted lattice parameters, saturation magnetic moments, and Curie temperatures are summarized in Table II.

We find that across the composition range studied that these alloys have a very low Rhodes-Wohlfarth ratio, which like the Slater-Pauling rule has been taken as another indirect sign of potential half-metallic behavior [11,39–41]. The Rhodes-Wohlfarth ratio is defined as p_c/p_s, where p_c is the effective paramagnetic moment per atom deduced from the Curie constant and p_s is the saturation moment extrapolated to $T = 0$ K. The Rhodes-Wohlfarth ratio is also useful in ascertaining the type of magnetism present in a material; for local moment ferromagnets, one expects a ratio $p_c/p_s = 1$, whereas for itinerant ferromagnets a ratio of greater than one is expected. On the other hand, in the case of half-metals, the ratio is expected to be substantially less than unity, which can be explained neither by itinerant nor by the localized model of magnetism. In order to explain a ratio $p_c/p_s < 1$, Otto *et al.* [39] proposed a simple molecular field model by taking into account both the local moments and spin-polarized itinerant electrons. According to their model, the total magnetization has contributions from both local moments and the itinerant holes, and antiferromagnetic exchange interaction

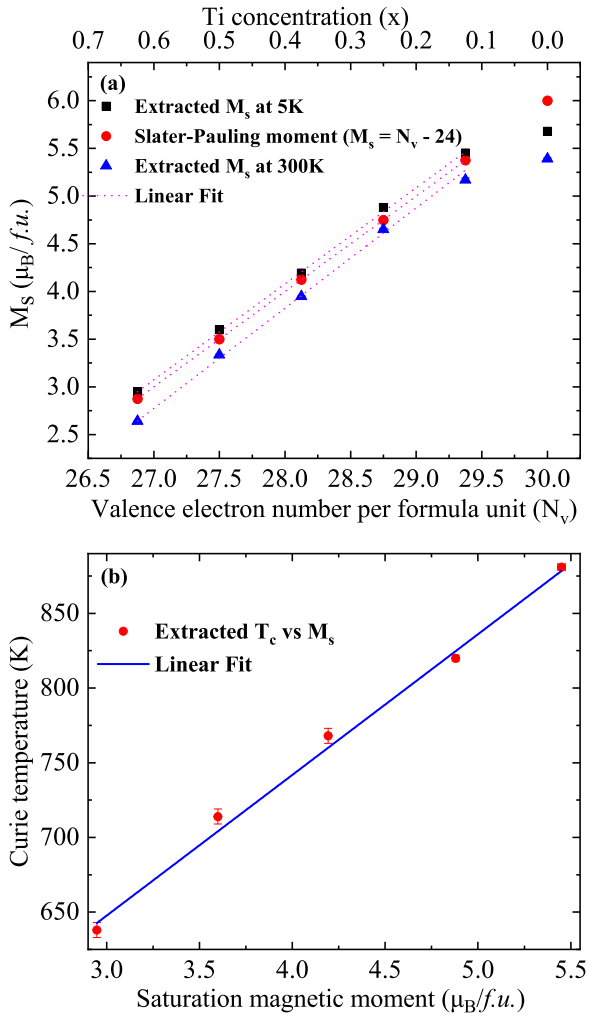

FIG. 9. (a) Comparison of extracted saturated magnetic moment with the expected moment from Slater-Pauling rule vs number of valence electrons. (b) Variation of Curie temperature as a function of saturation magnetic moment.

between the two reduces the Curie constant and therefore the p_c/p_s ratio. Within this model, "particularly small" values of p_c/p_s are expected for half-metallic ferromagnets. Their experimental data on NiMnSb predicted to be a half-metal by de Groot *et al.* [1], were consistent with the model proposed.

In a slightly different picture, however, Katsnelson *et al.* [11] explain the reduced Rhodes-Wohlfarth ratio in terms of a change of electronic behavior. In their picture, the reduction of moments in the paramagnetic regime is a consequence of a change in electron structure, and such a change is expected to be large in the case of half-metallic ferromagnets, thereby decreasing the p_c/p_s ratio below unity. In either picture, $p_c/p_s < 1$ is considered to be a novel property of half-metallic ferromagnets. In agreement with Katsnelson *et al.* [11] we consider this to be a preliminary, but clearly not sufficient, an indicator of potential half-metallic behavior making the system worthy of further study.

In order to determine the ratio p_c/p_s, p_s can be extracted from extrapolating saturation magnetic moment to 0 K, whereas p_c can be determined by using the relation, $p_c = \sqrt{1+\mu_{\text{eff}}^2} - 1$ [42]. The effective magnetic moment (μ_{eff}) can be deduced by using the following relation [39]:

$$C = \frac{N_a \mu_{\text{eff}}^2}{3Mk_B}, \tag{1}$$

where M is the molecular weight, k_B is the Boltzmann constant, N_a is Avogadro's number, and C is Curie constant which can be deduced from a fit to the Curie-Weiss law. The temperature-dependent magnetization data above T_c were fit to the Curie-Weiss law, as shown in Fig. 10. In general, the magnetic susceptibility above T_c follows the Curie-Weiss law with different slopes. This sort of deviating behavior of the magnetic susceptibility has been observed previously for several Heusler alloys [39,43,44] and is attributed to a decrease of the effective magnetic moment and an increase of paramagnetic Curie temperature with increasing temperature. Nonlinear behavior of the inverse susceptibility is observed in our samples (see Fig. 10), however, the nonlinearity is more pronounced (a plateau region is present) in the alloys with the higher Ti concentrations. For such samples, the effective magnetic moment was extracted separately for two regions (A and B in Fig. 10), and a reduction of the effective moment was indeed obtained at higher temperature, as explained above. The plateau can be observed in the usual M versus T plot as well when plotting the magnetization axis on a log scale (see Ref. [27] for details). However, the exact cause of this behavior is not clear at this point. Nonetheless, the p_c/p_s ratio, which is the quantity of interest here, was found to be well below unity in every case. This further corroborates our prediction of potential half-metallic behavior in the samples. The extracted effective magnetic moment, paramagnetic Curie temperature and p_c/p_s is displayed in Table III.

While the spontaneous magnetization curve follows the Brillouin function reasonably well at high temperatures,

TABLE II. Experimental lattice parameter and the saturation magnetization of $Co_{2-x}Ti_xFeGe$ ($0 \leqslant x \leqslant 0.625$) annealed at 950 °C for 3 days. As a comparison, the expected moment from following the Slater-Pauling (S-P) rule is also given. The number in parenthesis () is the uncertainty in the last digit.

Sample	a (Å)	S-P (μ_B/*f.u.*)	M_s(T = 5 K, μ_B/*f.u.*)	T_c (K)	Ref.
Co_2FeGe	5.742(2)	6.000	5.68(2)	981	[21]
$Co_{1.875}Ti_{0.125}FeGe$	5.753(2)	5.375	5.45(2)	881(2)	this work
$Co_{1.75}Ti_{0.25}FeGe$	5.762(2)	4.750	4.88(2)	820(2)	this work
$Co_{1.625}Ti_{0.375}FeGe$	5.770(2)	4.125	4.19(1)	768(5)	this work
$Co_{1.500}Ti_{0.5}FeGe$	5.782(1)	3.500	3.59(1)	714(5)	this work
$Co_{1.375}Ti_{0.625}FeGe$	5.789(1)	2.875	2.95(1)	638(5)	this work

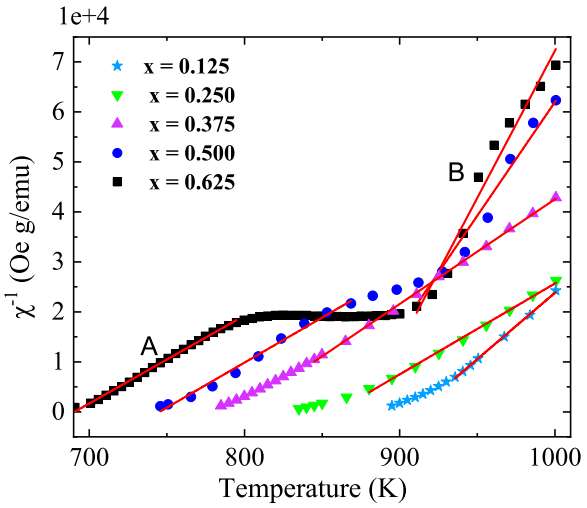

FIG. 10. Inverse susceptibility as a function of temperature for the alloys ($0.125 \leqslant x \leqslant 0.625$). The solid line is Curie-Weiss law fit.

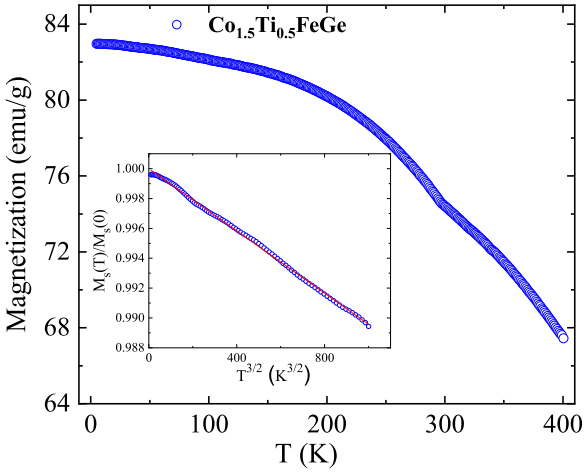

FIG. 11. Temperature-dependent magnetization curve measured in the range 4–400 K at 1 T for $Co_{1.5}Ti_{0.5}FeGe$. The inset graph shows the data for $T < 100$ K as function of $T^{3/2}$. The solid line is a linear fit to the experimental data showing $T^{3/2}$ dependence of magnetization at low temperature.

at low temperatures, the curve should follow the expression $M_s(T) = M(0)(1 - AT^{3/2})$ based on spin-wave theory, the so-called Bloch $T^{3/2}$ law [45]. This model fit is useful in extracting the spin-wave stiffness coefficient D in the spin-wave dispersion relation $\hbar\omega = Dq^2$, with $A = 2.612(V/S)(k_B/4\pi D)^{3/2}$ [39,46]. In this relationship, V is the volume per magnetic atom, S is the spin, and k_B is the Boltzmann constant. Knowledge of the spin-wave stiffness coefficient is important as it relates to the thermal stability of exchange interactions, and also affects the performance of spintronic devices. The fitting of low-temperature data in the case of $Co_{1.5}Ti_{0.5}FeGe$ (see Fig. 11) yielded a best fit value for A of $1.043 \pm 0.007 \times 10^{-5}$ $K^{-3/2}$. With this value of A, the corresponding value of D was calculated to be 287.3 meV Å^2. This value of D is comparable to the value of other known half-metallic full Heuslers [47,48] and half Heuslers [49].

Knowledge of magnetic anisotropy is also critical for most practical applications. However, determining the magnetic anisotropy in these bulk polycrystalline samples with irregular shapes is problematic. In order to gain some rough insight into the magnetic anisotropy of these alloys, we utilized the singular point detection technique (SPD) [50]. In the SPD technique, the anisotropy field H_a is determined by performing successive derivatives of the magnetization-field curves. While the order of the derivative depends on the particular symmetry of the specimen, in case of cubic crystals the singularity is usually observed in second or third derivatives [50]. Hence, from the $\frac{d^2M}{dH^2}$ versus H plot, an anisotropy field H_a of $\approx 2.3 \times 10^5$ A/m was determined. Then, with $M_s = 7 \times 10^5$ A/m and by using the relation $K_\mu = \frac{\mu_0 H_a M_s}{2}$, an estimated value of $\approx 1 \times 10^5$ J/m^3 was obtained for K_μ. Again, we stress that our samples are polycrystalline, making this an effective anisotropy at best, and given the irregular sample shape, we are unable to correct for demagnetization. However, we have recently made epitaxial thin films of the $x = 0.500$ composition, where these issues are not present, and ferromagnetic resonance measurements yield a very similar in-plane anisotropy value. The growth and characterization of thin films in this alloy series will be reported in a subsequent paper.

TABLE III. The effective magnetic moment above T_c, the paramagnetic Curie temperature θ, and p_c/p_s for the alloys ($0.125 \leqslant x \leqslant 0.625$). The number in parenthesis () indicates uncertainty in the last digit.

Sample	μ_{eff} (μ_B/*f.u.*)	θ (K)	p_c (μ_B/*f.u.*)	p_c/p_s
$Co_{1.875}Ti_{0.125}FeGe$	2.75(6)	907(1)	1.93(4)	≈0.35
$Co_{1.75}Ti_{0.25}FeGe$	3.26(6)	859(2)	2.41(4)	≈0.49
$Co_{1.625}Ti_{0.375}FeGe$	3.07(3)	793(1)	2.22(2)	≈0.53
$Co_{1.5}Ti_{0.5}FeGe$(A)	3.3(1)	746(3)	2.45(7)	≈0.67
$Co_{1.5}Ti_{0.5}FeGe$(B)	2.1(2)	864(9)	1.3(1)	≈0.36
$Co_{1.375}Ti_{0.625}FeGe$(A)	3.29(3)	690(1)	2.44(2)	≈0.83
$Co_{1.375}Ti_{0.625}FeGe$(B)	1.9(1)	868(5)	1.15(6)	≈0.39

4. Electrical transport measurement

The electrical transport properties were measured using the van der Pauw method [51]. The samples utilized had approximate dimensions of 5 mm × 5 mm × 2 mm. The electrical resistivity was measured in the temperature range of 5–400 K during both heating and cooling cycles. In the case of normal ferromagnets, the scattering of conduction electrons is mainly governed by three factors: scattering due to lattice defects (ρ_0), scattering due to lattice vibrations (ρ_{ph}), and scattering due to magnon excitations (ρ_{mag}). Hence the total resistivity of a magnetic alloy can be expressed by following Matthiessen's rule [52] as

$$\rho(T) = \rho_0 + \rho_{\text{ph}}(T) + \rho_{\text{mag}}(T) \quad (2)$$

The phononic contribution to the resistivity can be modeled with the Bloch-Grüneisen formula:

$$\rho_{\rm ph}(T) = \alpha\left(\frac{T}{\Theta_D}\right)^5 \int_0^{\frac{\Theta_D}{T}} \frac{x^5}{(e^x-1)(e^{-x}-1)}dx. \quad (3)$$

The magnetic contribution is rather complicated. In general, a T^2 variation is expected due to one magnon scattering. However, in half-metals, due to the presence of a gap in one of the spin channels the T^2 variation is assumed to be exponentially suppressed (i.e., no spin-flip scattering) at low temperature [53]. Thus, in the case of half-metals, the usual electron-magnon scattering could be modified by including a Boltzmann factor as [54,55]

$$\rho_{\rm mag}(T) = \beta T^2 e^{-\Delta/T}, \quad (4)$$

where Δ measures the energy gap between the Fermi level and the band edge of the unoccupied band. We chose only the samples with $x = 0.375$ and 0.500 for transport measurements, as compositions in this range showed good single-phase microstructure and excessive grain boundaries in the other samples further complicate interpretation. The temperature variation of resistivity is shown in Fig. 12. Metallic behavior was observed for all samples. The residual resistivity (ρ_0) is relatively high in all samples. The large residual resistivity is most readily attributed to scattering at grain boundaries, impurities, and pores as seen in higher magnification in SEM, but may also indicate a substantial degree of atomic disorder (which we are not able to quantify via XRD as noted above). The residual resistivity ratio (RRR) of ≈1.2 further indicates that the sample quality was not ideal for transport experiments.

As shown in Fig. 12, the resistivity decreases with the decreasing temperature down to 50 K. Below 50 K, the resistivity was found to be nearly constant. The experimentally measured data could be fitted over the entire temperature range using Eq. (2) incorporating phononic and magnonic parts from Eqs. (3) and (4), respectively. The insets in Fig. 12 display the fitting in the low-temperature regime (<100 K), both with and without taking Boltzmann factor into consideration. It can be observed that inclusion of the Boltzmann factor resulted in a better fit for both samples. It reduced the chi-square value by an order of magnitude (see Fig. 12 for chi-square values). The Boltzmann factor was then used to determine the energy gap ($k_B\Delta$) which increases as we go from $x = 0.375$ to 0.500. The value of the energy gap and other best-fit parameters are displayed in Table IV. The increase of energy gap suggests that the Fermi level shifts left from the band edge of the minority conduction band with increasing Ti content. Such a behavior can be related to the expansion of the lattice with Ti concentration, which shifts the Fermi level deeper in energy. This behavior also agrees qualitatively with our theoretical findings, which will be discussed below in Sec. III. These findings lend some support to our argument that there is half-metallic behavior in the intermediate composition ($x \approx 0.500$).

Although the resistivity measurement and fit are consistent with the idea suggested by Galanakis *et al.* [25] (that lattice expansion shifts Fermi level deep in energy) and our theoretical findings, the conclusion that this implies half-metallicity should be considered speculative since the data can also be fit very well without including the exponential term at all. More to the point: *of course,* the fit is likely to be better when adding another free parameter, this does not necessarily imply the model is correct. Further experiments with high-quality single crystal samples are necessary to draw more reliable conclusions from the transport properties.

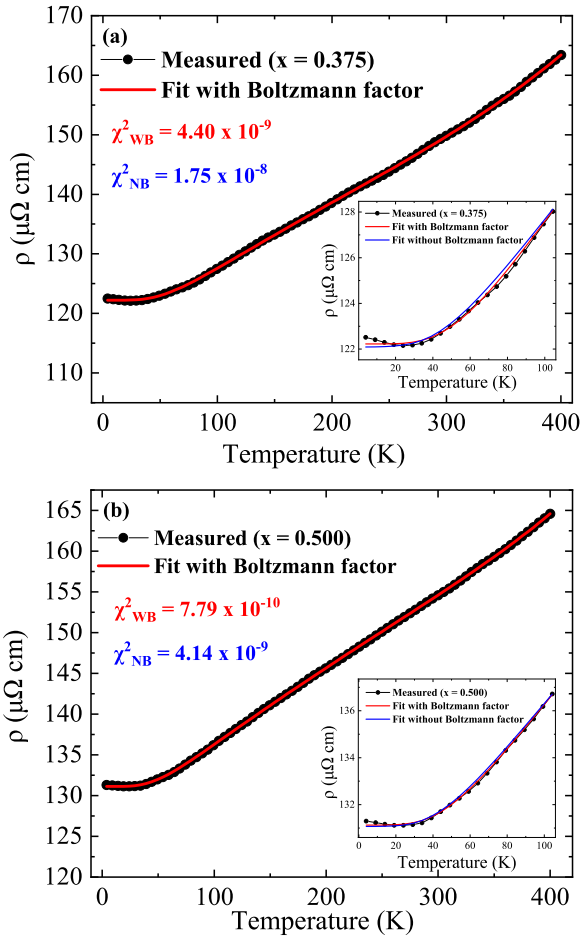

FIG. 12. Temperature dependence of resistivity in zero magnetic field for (a) $Co_{1.625}Ti_{0.375}FeGe$ and (b) $Co_{1.5}Ti_{0.5}FeGe$. The insets in figure show fit of low-temperature data with and without considering the Boltzmann term in the magnon scattering. The reported χ^2 values are obtained from the fit while including the Boltzmann factor (WB) and while not including the factor (NB).

5. Mechanical properties

It became apparent while preparing these alloys for metallography that they are unusually hard. Hardness data on Heusler alloys are relatively scarce, particularly for full Heusler alloys. Further, several Heusler alloys have attracted attention for thermoelectric applications, which requires good mechanical robustness to withstand repeated thermal cycling. Based on our initial observations an investigation of the hardness of these alloys seemed warranted. Rogl *et al.* [56] summarized the mechanical properties of half-Heusler alloys, with the hardest alloys exhibiting Vicker's hardness of 10–14 GPa. For full Heuslers, Hakimi *et al.* [57] studied the hardness of

TABLE IV. Fitted parameters of resistivity data for samples with $x = 0.375$ and 0.5.

Sample	Θ_D (K)	ρ_0 ($\mu\Omega$ cm)	α ($\mu\Omega$ cm)	β ($\mu\Omega$ cm K^{-2})	Δ (K)	$k_B\Delta$ (eV)
$Co_{1.625}Ti_{0.375}FeGe$	339(4)	122.22(4)	$4.3(1) \times 10^4$	$0.9(2) \times 10^{-3}$	1400(103)	0.12(1)
$Co_{1.5}Ti_{0.5}FeGe$	303(2)	131.12(2)	$3.03(4) \times 10^4$	$3(1) \times 10^{-3}$	2400(176)	0.20(2)

nanocrystalline Co_2FeAl powder, finding a Vicker's hardness of up to ≈8.5 GPa, while Ouardi *et al.* [58] reported ≈7.3 and ≈7.9 GPa for bulk polycrystalline Co_2MnGe and Co_2MnSi, respectively.

The hardness of the heat treated samples was measured in a Buehler model 1600-6100 hardness tester using the Vickers technique. In this technique, an impression is made with a square-based diamond-pyramid indenter and the length of the diagonals of the impression is measured to calculate the hardness in terms of the Vickers number (H_v). The results of hardness measurement performed for all the samples in the series ($0 \leqslant x \leqslant 1$) are shown in Fig. 13. At least ten indents were made for each sample to improve the accuracy of the measurement. A significant enhancement in hardness with increasing Ti concentration is observed. An increase of hardness is anticipated with the substitution of atoms with a larger atomic radius for the atoms with a lower atomic radius [59], consistent with our substitution of Ti for Co. Similarly, hardness is found to depend strongly on porosity, grain size and on the phase separation [56]. From the microstructure analysis, a decrease in grain size is observed on going from $x = 0$ to 0.500. We argue that grain size reduction is one of the key factors in the enhancement of hardness. In the case of $x = 0.625$, the grain boundaries were invisible which correlated with a slight downturn in the hardness. From $x = 0.625$ to 1, however, microstructure analysis indicated the presence of multiple-phases, thereby enhancing the hardness even further. In Fig. 13, for the single-phase region and multi-phase region, two different regimes of hardness enhancement can be observed. This is expected as the source of hardness is different for these regimes; for instance, grain size reduction enhances the hardness for single-phase samples, whereas phase segregation is a key factor in the case of multi-phase samples. For high

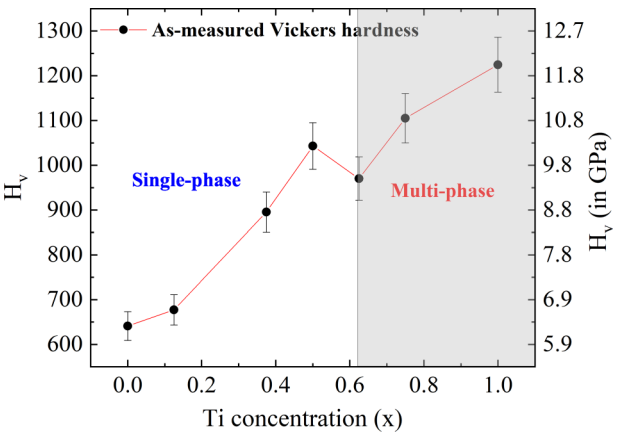

FIG. 13. Measured hardness value for the alloys in the series ($0 \leqslant x \leqslant 1$). Slightly different trend of hardness increment can be seen for the single-phase and multiphase samples.

Ti concentration, the observed hardness is substantially larger than those reported for Co_2MnSi or Co_2MnGe (or typical values for hardened steel, for example), and compares favorably with the hardest reported half-Heusler alloys. Exploration of different processing conditions to optimize the microstructure may allow a substantial increase in hardness.

III. THEORETICAL APPROACH

To briefly summarize our experimental results; although it seems to be difficult to synthesize a single-phase Co_2FeGe $L2_1$ compound, substitution of Ti for Co, i.e., $Co_{2-x}Ti_xFeGe$ for $0.125 \leqslant x \leqslant 0.625$ allowed us to obtain single-phase materials with XRD patterns consistent with $L2_1$. However, the transition elements, especially Co and Fe, scatter x rays so similarly that although we are confident there is an fcc superstructure on the bcc base structure, it is not clear how the Co, Fe, and Ti atoms are arranged. In this section, we describe calculations using density functional theory (DFT) aimed at obtaining further information about the likely structure.

A. Calculation details

We have calculated the zero-temperature electronic structure, magnetic structure, physical structure and relative energies of a number of possible $Co_{2-x}Ti_xFeGe$ structures. These calculations were performed using 16-atom supercells, i.e., 4 formula units of the underlying $L2_1$ compound. The calculations employed DFT as implemented in the Vienna *ab initio* simulation package (VASP) code [60] which uses projector augmented wave (PAW) pseudopotentials [61]. The Perdew-Burke-Ernzerhof (PBE) version of the generalized gradient approximation (GGA) was used for exchange and correlation [62]. The calculations were performed using 64 k points in the irreducible zone of the supercell. The energy cutoff for the plane wave basis set was 520 eV. The (initially cubic) cell dimensions and the atomic positions within the cell were relaxed using the conjugate-gradient method. Our calculations did not include spin-orbit interaction. The results of our calculations are summarized in Table V.

Although we calculate zero-temperature energies and magnetic moments, we intend to use them to make inferences about the relative free energy of different configurations of the atoms in these materials at annealing temperatures on the order of 1200 K where the atoms are sufficiently mobile to achieve the minimum free energy configuration during the 3-day annealing period. Differences in entropic contributions to the free energy will arise from the dependence of lattice vibrations and magnetic excitations on the atomic configurations. In addition, there will be a contribution to the free energy from the antisite disorder that will ensure some degree

TABLE V. DFT calculation results for some possible atomic configurations. In the table E, E_L, M, M_{SP}, and $\langle a \rangle$ represent calculated energy, energy of most stable configuration, calculated moment, Slater-Pauling moment, and optimized lattice parameter.

Configuration	4a	4b	4c	4d	$E - E_L$ (eV)	M ($\mu_B/f.u.$)	$M - M_{SP}$ ($\mu_B/f.u.$)	⟨a⟩ (Å)	Tet. (a/c -1)
$x = 0$									
Co_8-Fe_4Ge_4	4Co	4Co	4Fe	4Ge	0	5.7010	−0.2990	5.7475	0.000
Co_7Fe-Fe_3CoGe_4	1Fe,3Co	4Co	1Co,3Fe	4Ge	0.2396	5.0850	−0.9148	5.7266	0.000
Co_7Ge-Fe_4CoGe_3	1Ge,3Co	4Co	4Fe	1Co,3Ge	1.8915	5.0375	−0.9625	5.7694	0.011
$x = 0.25$									
Co_7Fe-Fe_3TiGe_4	1Fe,3Co	4Co	1Ti,3Fe	4Ge	0	4.7110	−0.0389	5.7710	0.000
Co_7Ti-Fe_4Ge_4	4Co	1Ti,3Co	4Fe	4Ge	0.9101	4.7460	−0.0039	5.7928	0.000
Co_7Ge-Fe_4TiGe_3	1Ge,3Co	4Co	4Fe	1Ti,3Ge	2.5386	4.6810	−0.0691	5.8196	0.000
$x = 0.5$									
Co_6Fe_2-$Fe_2Ti_2Ge_4$	1Fe,3Co	1Fe,3Co	2Ti,2Fe	4Ge	0	3.4995	−0.0005	5.7861	−0.013
Co_5Fe_3-$CoFeTi_2Ge_4$	1Fe,3Co	2Fe,2Co	1Co,2Ti,1Fe	4Ge	0.5638	2.8335	−0.6665	5.7722	0.005
Co_6FeTi-Fe_3TiGe_4	1Fe,3Co	1Ti,3Co	1Ti,3Fe	4Ge	1.1019	3.5470	0.0466	5.8112	−0.006
Co_4Fe_4-$Co_2Ti_2Ge_4$	4Co	4Fe	2Ti,2Co	4Ge	1.1203	2.2784	−1.2217	5.7521	0.011
$Co_4Fe_2Ti_2$-$Co_2Fe_2Ge_4$	2Fe,2Ti	4Co	2Fe,2Co	4Ge	1.9135	2.7250	−0.7749	5.8081	0.473
$Co_2Fe_4Ti_2$-Co_4Ge_4	2Fe,1Ti,1Co	2Fe,1Ti,1Co	4Co	4Ge	1.9985	2.6060	−0.8943	5.7901	0.559
Co_6Ti_2-Fe_4Ge_4	1Ti,3Co	1Ti,3Co	4Fe	4Ge	2.4155	4.2920	0.7920	5.8576	0.000
Co_5Ti_2Fe-$CoFe_3Ge_4$	1Ti,1Fe,2Co	1Ti,3Co	1Co,3Fe	4Ge	2.6961	3.4904	−0.0096	5.8299	−0.020
$Fe_4Co_2Ti_2$-Co_4Ge_4	4Fe	2Ti,2Co	4Co	4Ge	2.9207	3.4190	−0.0808	5.8298	−0.090
$Co_4Fe_2Ti_2$-$Co_2Fe_2Ge_4$	1Fe.1Ti,2Co	1Fe,1Ti,2Co	2Co,2Fe	4Ge	3.0697	2.9843	−0.5157	5.8123	−0.054
$x = 0.75$									
Co_5Fe_3-$FeTi_3Ge_4$	2Fe,2Co	1Fe,3Co	3Ti,1Fe	4Ge	0	2.2500	0	5.8001	−0.011
Co_4Fe_4-$CoTi_3Ge_4$	4Co	4Fe	1Co,3Ti	4Ge	0.5701	1.4627	−0.7874	5.7800	0.000
Co_5FeTi_2-$TiFe_3Ge_4$	1Fe.1Ti,2Co	1Ti,3Co	1Ti,3Fe	4Ge	2.6404	3.4156	1.1656	5.8735	−0.012
Co_5Ti_3-Fe_4Ge_4	2Ti,2Co	1Ti,3Co	4Fe	4Ge	2.9803	3.4443	1.1943	5.8989	0.006
x = 1.0									
Co_4Fe_4-Ti_4Ge_4	4Fe	4Co	4Ti	4Ge	0	1	0	5.8156	0.000
Co_4Ti_4-Fe_4Ge_4	2Ti,2Co	2Ti,2Co	4Fe	4Ge	2.8114	0.8055	−0.1945	5.8673	0.528
Co_4Ti_4-Fe_4Ge_4	4Ti	4Co	4Fe	4Ge	3.6451	2.9978	1.9978	5.9458	0.000
Co_4Ge_4-Fe_4Ti_4	4Co	4Ge	4Fe	4Ti	6.1077	0	−1	5.8805	0.000

of randomness in the site occupations. These uncertainties are in addition to any errors inherent in the use of a mean-field treatment of electronic structure.

Fortunately, we have some experience that may be useful in our attempt to gain insight into which of the phases consistent with the experimental data are more likely. Ma *et al.* [63] investigated all inverse Heusler alloys reported as stable in the Inorganic Crystal Structure Database (ICSD) [64,65] and more recent literature. They found that DFT-calculated energies of the stable phases were within 0.052 eV/atom of the DFT-calculated convex hull. In other words, most of the experimentally stable inverse Heusler alloys were found to be lower in DFT-calculated energy than competing phases. The competing phases were drawn from the Open Quantum Materials Database [66,67] which contains more than 500 000 phases. Those that were not lower in calculated energy than all other phases or combination of phases in the database, yet were observed experimentally, were within 0.052 eV/atom in energy from the energy of that phase or combination of phases.

We assert that although entropic contributions to the free energy will certainly be different for different phases, calculated energy differences between structures in excess of about 0.05 eV/atom can be used to indicate which phase, consistent with available experimental data, is more likely.

Additional valuable information is provided by the calculated spin moments. The experimental moments of the $Co_{2-x}Ti_xFeGe$ alloys vary linearly over the range where single-phase materials have been synthesized, the magnitudes being slightly greater than the value expected for a Slater-Pauling half-metal with three electrons per atom in the minority channel. These moments and their variation with concentration are only consistent with the DFT calculations (within experimental error and allowances for possible orbital moments) if the Ti atoms occupy the 4c sites.

Below we discuss the calculations which are summarized in Table V. In describing the atomic configurations, we will use the occupation of the Wyckoff positions of Space group 216 (structure Y). Thus the compound, CoFeTiGe, generates a 16 atom computational supercell in which four Co atoms, four Fe atoms, four Ti atoms, and 4 Ge atoms occupy the 4a, 4b, 4c, and 4d sites of structure Y. We will also sometimes refer to the A and B sublattices. The A sublattice consists of the 4a and 4b sites. The B sublattice comprises the 4c and 4d sublattices. The A and B sublattices (before relaxation) are both simple cubic lattices. Every atom on the A sublattice is at the center of a cube with eight B-lattice atoms at the corners and every atom on the B sublattice is at the center of a cube with eight A-lattice atoms at the corners. This structure in which nearest neighbors of A atoms are B atoms

and vice versa makes possible hybridization gaps near the center of the *d* band often seen in the density of states (DOS) of Heusler alloys. Relaxation of the structures to eliminate the forces on the atoms will reduce the symmetry of the cells because many of the configurations do not have cubic symmetry. Most of these distortions are of the order of a few percents or less. A few configurations, however, relaxed to structures quite different from the initial ones and inconsistent with the experimental XRD data. In Table V, the energy, moment, and lattice constant in the table refer to the 16 atoms computational cell after relaxation starting from a cubic cell.

B. Results and discussion

1. Co_2FeGe

Three calculations were performed for the composition Co_2FeGe, one for the base $L2_1$ compound, one in which an Fe and a Co atom were interchanged and one in which a Ge and a Co atom were interchanged. The DFT electronic structure of Co_2FeGe is similar to that of Co_2FeSi [68]. There is a gap in the minority DOS after 12 states per formula unit consistent with the Slater-Pauling rule, but with 30 electrons per formula unit, it is not energetically favorable for the Co and Fe atoms to generate the 6 Bohr magnetons of magnetic polarization needed to place the Fermi energy in the gap. The magnetization is 5.7 μ_B and the Fermi energy falls 0.15 electron/formula unit above the gap.

A simple explanation of why it is difficult for this compound to generate magnetization of 6 μ_B per formula unit is that Co only has about 1.6 unoccupied *d* states/atom and Fe only about 2.6, so 6 μ_B would require the energetically unfavorable occupation of *s* states above the top of the *d* complex by majority electrons. This simple explanation is based on the following *s*-*d* model construction. Co and Fe have nine and eight electrons respectively. The ten *d* states per atom are more or less degenerate with a broad *s* band that will hold, approximately 0.5 electrons per atom below the Fermi energy more or less equally distributed between up and down spin channels. There remain about 8.5 and 7.5 *d* electrons per Co and Fe atom respectively, leading to maximum moments of about 1.5 and 2.5 μ_B per atom. The maximum moments can vary slightly depending on the relative positions of the *s* and *d* bands and amount of charge transfer between atoms

Interchange of one of the four Fe atoms with one of the eight Co atoms in the 16-atom computational supercell costs an energy of 0.24 eV, reduces the magnetic moment by 2.46 μ_B and eliminates the Slater-Pauling gap. Interchange of one of the four Ge atoms with one of the eight Co atoms in the computational cell costs 1.89 eV and reduces the magnetic moment by 2.65 μ_B. It also eliminates the gap in the DOS. Comparison of these two interchange energies indicates that Co-Fe interchange is much more likely than Co-Ge interchange.

2. $Co_{1.75}Ti_{0.25}FeGe$

Possible phases with $x = 0.250$ were investigated in the 16-atom computational supercell using three calculations: (a) one of the eight Co atoms is replaced by a Ti atom, and (b) A Co atom is removed and a Ti atom is added, but the Ti atom displaces an Fe atom going to the site vacated by the removed Co atom. (c) The same as (b) but the Ti goes to a Ge site with the displaced Ge atom going to the vacant Co site. Configuration (b) has the lowest energy. Configuration (a) is higher by 0.91 eV and configuration (c) is higher by 2.54 eV. We infer from this result that at low concentrations, Ti prefers to replace Fe on the FeGe sublattice. We also confirm the XRD results that the Ge atoms form an fcc superstructure on the underlying bcc lattice.

All three of the calculations yield a moment close to the Slater-Pauling value of 19 μ_B per 16-atom computational cell. Calculation (a) in which a Ti atom simply replaces a Co atom yields 18.98 μ_B, (b) in which Ti replaces an Fe which is displaced to the vacant Co site yields 18.84 μ_B, while (c) in which Ti replaces a Ge atom yields 18.72 μ_B. The DOS for calculation (b) appears very similar to that for Co_2FeGe with the exception that the Fermi energy is much closer to the energy gap with the Ti substituting for Fe. The DOS for calculation (a) shows the Fermi energy in a very small region of very low density of states. However, we predict a pseudogap rather than an actual gap. There is no sign of a Slater-Pauling gap after three electrons per atom when Ti substitutes for Ge.

Compared to Co_2FeGe, the calculated lattice constant of $Co_{1.75}Ti_{0.25}FeGe$ is calculated to increase by 0.023, 0.045, or 0.071 Angstrom depending on whether the Ti substitutes for Fe, Co, or Ge, respectively. The increase in experimental lattice constant is 0.020 Å.

3. $Co_{1.5}Ti_{0.5}FeGe$

Ten atomic configurations were calculated for $Co_{1.5}Ti_{0.5}FeGe$ as shown in Table V. The atomic configuration with the lowest calculated energy has Co and Fe on sublattice A (4a and 4b sites) with Fe, Ti, and Ge on sublattice B (4c and 4d sites). This configuration is predicted to generate a "near-half-metal" with a minority gap of slightly less than 0.1 eV. The Fermi energy is predicted to fall just above the bottom of the conduction band in a region of extremely low DOS. The predicted spin moment is only 0.002 μ_B less than the Slater-Pauling value of 14 μ_B.

The next lowest energy configuration again has only Co and Fe on the A sublattice, but one Co atom on the A sublattice has been swapped with an Fe atom on the B sublattice. This interchange costs 0.56 eV and reduces the calculated magnetic moment by 2.66 μ_B.

The third lowest energy configuration has one Ti on the A sublattice and one on the B sublattice while all of the Co is on the A sublattice. This configuration is higher in energy by 1.10 eV than the minimum energy configuration and the moment is also slightly larger. There is a very narrow dip in the DOS above the Fermi energy with a Slater-Pauling gap of about 0.01–0.02 eV in width.

Almost degenerate in energy with the last configuration is a configuration with equal amounts of Co and Fe on sublattice A, and Co, Ti and Ge on sublattice B. There is another narrow gap in the DOS well below the Fermi energy at 36 minority electrons per 16 atom cell (2.25 minority electrons per atom). The moment of this configuration is less than the Slater-Pauling value by nearly 5μ_B.

Next higher in energy are two configurations that relaxed to highly tetragonal structures. The relaxed structures have little relation to the starting structures with, for example, completely different nearest neighbors.

Next higher in energy among the investigated configurations is the one that represents simple substitution of Ti for Co. It is 2.42 eV higher in energy than the lowest energy configuration. Its moment is 3.17 higher than the Slater-Pauling value. The DOS shows no sign of a Slater-Pauling gap.

Next higher in energy above simple substitution is a configuration that can be considered simple substitution of Co by Ti plus an interchange of one of the remaining Co atoms on the A sublattice with an Fe atom on the B sublattice. This interchange costs an additional 0.28 eV of energy compared to simple substitution. The calculated moment differs from the Slater-Pauling value by about 0.04 but there is no Slater-Pauling gap.

Calculations were performed for two additional configurations with Ti on the A sublattice and more Co on the B sublattice. The energies were about 3 eV higher than the minimum energy configuration and they had tetragonal distortions of about 5% and 9%.

To summarize the calculations for $x = 0.500$, the lowest energy configuration has all Co atoms on the A sublattice and all Ti and Ge on the B sublattice. Interchange of an Fe and a Co such that one of the Co atoms sits on the B sublattice costs about 0.56 eV. The "simple substitution" configuration in which a Ti occupies the site of a missing Co on the A sublattice is higher in energy by about 2.42 eV. The lowest energy state is a Slater-Pauling "near-half-metal" with about 0.002 electrons in the conduction band.

4. $Co_{1.25}Ti_{0.75}FeGe$

Four configurations with $x = 0.750$ were investigated. The lowest energy configuration (Co_5Fe_3-$FeTi_3Ge_4$) had all three Ti atoms on the B sublattice with all of the Co on the A sublattice. This configuration is predicted to be a Slater-Pauling half-metal.

The next highest energy configuration (Co_4Fe_4-$CoTi_3Ge_4$) also had all three Ti atoms on sublattice B, but compared to the lowest energy configuration, one of the Co atoms on sublattice A had been swapped with an Fe on sublattice B. This interchange cost 0.57eV and reduced the magnetic moment by 3.15 μ_B.

The next highest-energy configuration (Co_5FeTi_2-$TiFe_3Ge_4$) had all of the Co atoms and 2/3 of the Ti atoms on the A sublattice. It was higher in energy than the lowest calculated configuration by 2.64 eV and had a larger moment by 4.66 μ_B.

The highest energy configuration calculated was that of simple substitution of Co by Ti on the A sublattice. Compared to the minimum energy configuration, it was higher in energy by 2.98 eV, and higher in moment by 4.78 μ_B.

5. CoTiFeGe

Three possible phases of CoTiFeGe with space group 216 are possible. If Co is assigned the 4a Wyckoff position, then the 4b position may be one of Fe, Ti, or Ge. The 4a and 4b positions can be thought of as forming one sublattice (A) while the 4c and 4d positions form a second sublattice (B). All of the nearest neighbors of an atom on sublattice A are on sublattice B and vice versa. Of these three phases, the phase in which Co and Fe are on one sublattice, (e.g., A) and Ti and Ge are on the other (e.g., B) has the lowest energy, −118.155 eV. Putting Co and Ti on the same sublattice increases the energy by 3.645 eV or 0.228 eV/atom. Putting Co and Ge on the same sublattice increases the energy by 6.108 or 0.382 eV/atom. CoFeTiGe with Co and Fe on the A sublattice is predicted by DFT to be a Slater-Pauling half-metal in agreement with Refs. [32,33].

One additional calculation was performed in which the Co and Ti atoms occupied the A sublattice and Fe and Ge occupied the B sublattice, but the cubic symmetry of space group 216 was broken by allowing the allowing both the 4a and 4b sublattices to be two Co and two Ti atoms. This system relaxed to a highly tetragonal structure allowing the Fe and Ge atoms to become nearest neighbors and the Co and Ti atoms to become nearest neighbors.

C. Conclusions from calculations

The experimental and theoretical calculations can be rationalized with the following picture. Although the chemical composition of the stable cubic phases of the Co-Ti-Fe-Ge system, $Co_{2-x}Ti_xFeGe$, appears to imply that the Ti atoms are substituting on Co lattice sites of the underlying Co_2FeGe system, it is more likely that Ti is substituting for Fe atoms which are displaced to the vacant Co sites. This picture is supported by the calculated energies (Table V). For all four of the Ti concentrations for which we performed calculations, the lowest energy structure had Co and Fe on the A sublattice and Ti, Fe and Ge on the B sublattice. The energies of the configurations with Ti on the B sublattice all had energies much lower (e.g., exceeding our empirical 0.05/atom threshold) than for Ti on the A sublattice. On the other hand, some configurations with a small amount of Co on the B sublattice cannot be ruled out energetically, because they are only slightly higher in energy than the minimum energy configurations. The best argument against these configurations is that they yield moments significantly below those measured experimentally.

Each of the minimum energy structures is a Slater-Pauling half-metal—or nearly so (see Fig. 14), giving a linear variation of the magnetic moment with the Ti concentration in agreement with experiment. The small systematic excess of the experimental moment above the Slater-Pauling value and the calculations may be due to orbital moments not included in the calculations or possibly systematic experimental error. Reference [27], provides the contribution of each element to the total magnetic moment as well as the number of electrons in the spin-up and spin-down channels calculated for the most stable configuration.

A simple explanation for the variation of the moment with Ti concentration and for the half-metallic nature of these phases can be given as follows [63,69]. The Slater-Pauling state in which a gap forms for $L2_1$ structures after 12 states per formula unit in one of the spin channels requires: (a) sufficient contrast between the position of the d states of the A and B sublattices in the gapped channel to open a hybridization

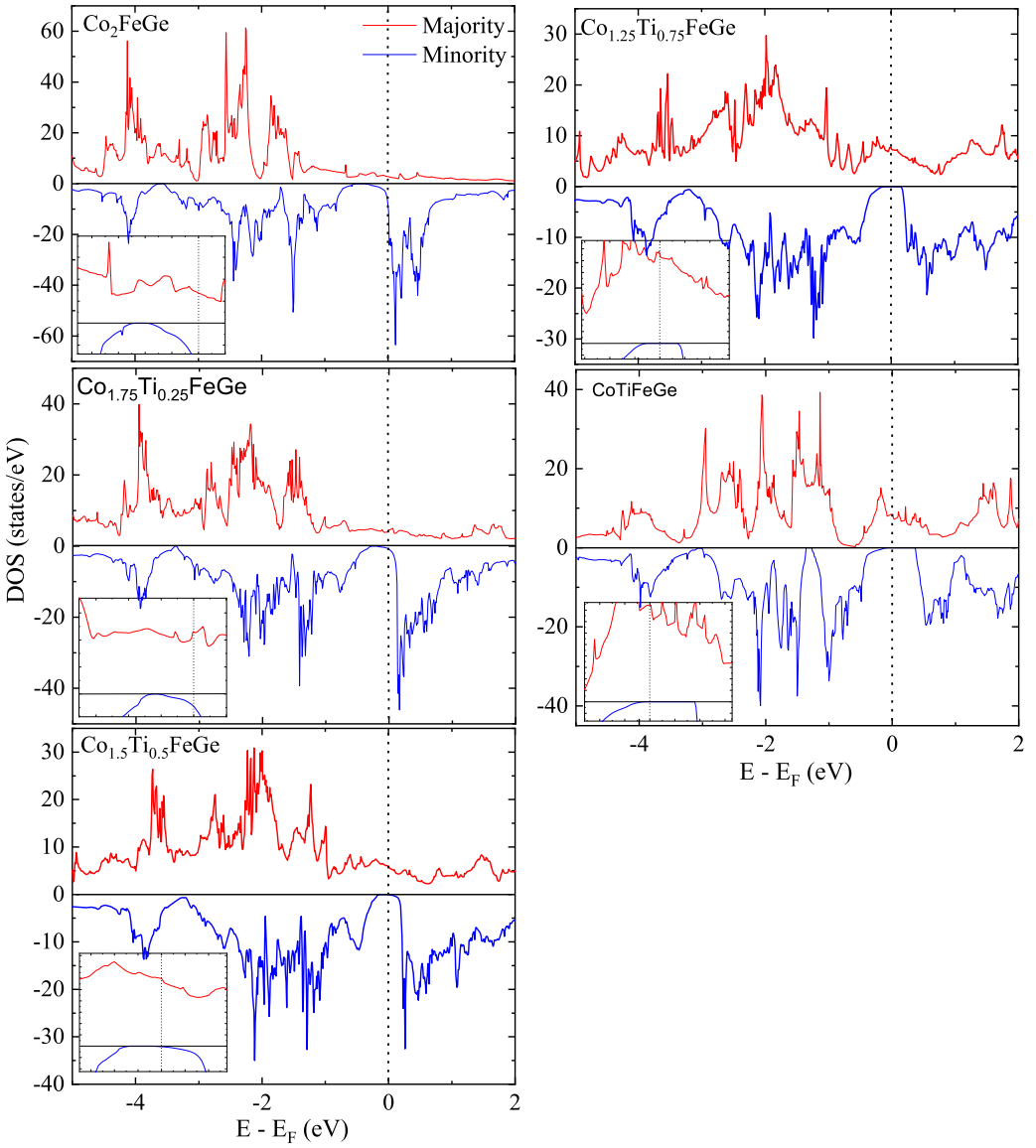

FIG. 14. Spin resolved density of states plot for $Co_{2-x}Ti_xFeGe$ ($0 \leqslant x \leqslant 1$) alloy series. It can be observed that Ti substitution for Co tunes a perfect half-metallic character in the parent Co_2FeGe alloy after $x > 0.500$. In the insets, the magnified view of the vicinity of Fermi level is shown to show relative position of the Fermi level with respect to the band gap.

gap between the *d* states of the transition metal atoms on the A sublattice and their nearest neighbors on the B sublattice, and (b) Sufficiently low symmetry that compatibility relations do not eliminate the gap. Empirically, Heusler type structures, especially the $L2_1$ phases are found to have both sufficiently low symmetry and the property that sublattice A has only B sublattice nearest neighbors and vice versa. B2 phases for example, have the property that A sublattice atoms have nearest neighbors that are on the B sublattice and vice versa, but the high symmetry usually means that the compatibility relations, i.e., how the bands connect the different symmetry points do not allow a gap near the center of the *d* band.

If the Fermi energy is to fall in this gap, the average number of electrons per atom in the gapped channel must be 3. The requirement for contrast between the *d* states on the two sublattices and the requirement that the average of the number of electrons on the two sublattices be exactly three constrains the possible configurations that can produce half-metals. Of the four types of atoms in the $Co_{2-x}Ti_xFeGe$ system, Ge has no *d* states and is thus nearly impossible to appreciably magnetically polarize. Likewise, although Ti has *d* states, they naturally lie rather high in energy and are also difficult to polarize. As a consequence, both Ti and Ge will have approximately two electrons in both the majority and minority spin channels. The low-lying *d* states of Co are narrow in energy and so tend to be magnetically polarized. The moment however, cannot be larger than about 1.5 without occupying majority states above the *d* bands. Such highly dispersive states are energetically expensive to occupy. Fe has a rather malleable moment that can vary from 0, e.g., in Fe_2TiSi to about 2.6, e.g., in Co-Fe alloys. Thus Fe atoms can occupy either the A sublattice or the B lattice without completely spoiling the half-metal feature of the band structure. It does this by having a small moment on the A sublattice (ideally

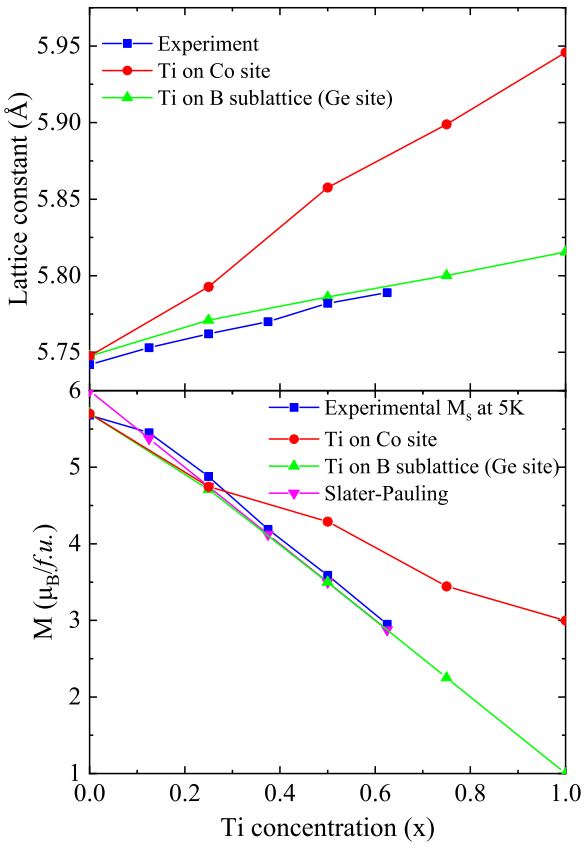

FIG. 15. Comparison of experimental and calculated lattice constants, magnetic moments with the Ti concentration. The experimental data for higher Ti concentration ($x > 0.625$) are not included, as those exhibited multiphase microstructure.

zero so that it has four minority channel electrons), and a large moment on the B sublattice (ideally three so that it has 2.5 minority electrons).

The calculated variation of the lattice constant and magnetic moment with Ti concentration is much closer to experiment for the minimum energy solutions (Ti displaces Fe to vacant site) than for simple substitution of Ti for Co as shown in Fig. 15.

IV. SUMMARY

In summary, from the bulk synthesis and characterization, single-phase microstructure in the $Co_{2-x}Ti_xFeGe$ alloy series were obtained by substituting Ti for Co, up to $x = 0.625$. XRD analysis of polycrystalline samples revealed a face centered cubic crystal structure for all single-phase samples with a linear increase of lattice parameter with Ti concentration, which is needed to shift the Fermi level deeper in energy and hence tune half-metallic behavior. Soft ferromagnetic behavior with extracted saturated magnetic moments agreeing well with Slater-Pauling behavior was observed, an indication of possible half-metallic behavior. Very high Curie temperatures with a seemingly linear relation with saturation magnetic moments were also obtained in case of single-phase samples. The linear dependence of M_s and T_c with the number of valence electron suggested that substituting the high-valent transition metal is another general approach that can be utilized to tune desired properties in Heusler alloys. The resistivity data could be fit including an exponentially decaying term in the magnon scattering factor. An increase of the extracted energy gap with an increase in Ti concentration was observed from the resistivity data fitting, in agreement with theoretical calculations and consistent with half-metallic behavior. A micro-hardness study revealed an enhancement in the hardness by a factor of 2 for high Ti concentration alloys compared to parent Co_2FeGe alloy, thereby making these alloys a potential candidate for mechanical applications. The theoretical calculations predicted atomic configuration in which the substituted Ti atom displaces Fe atom towards vacated Co site as the most stable configuration supported by the experimental findings. The theoretical calculations also predicted near half-metallic character in the intermediate substitution range ($x \approx 0.500$) and a perfect half-metallic behavior for $x \geqslant 0.750$.

ACKNOWLEDGMENTS

We would like to acknowledge Mark Weaver for helpful discussions on measurements of mechanical properties and for providing the instrument for hardness measurements. We would also like to acknowledge Bibekananda Das for helping us to carry out high-temperature magnetization measurements. This work utilizes the facilities operated by the Central Analytical Facility (CAF) and MINT Center of The University of Alabama. We are thus grateful to the members of CAF and MINT center for helping us with the instrumentation. The financial support to conduct this work was provided from National Science Foundation (NSF) Grants No. DMREF 1235396 and No. DMR 1508680. The authors are thus thankful to NSF for providing the funding support in successful completion of this work.

[1] R. De Groot, F. Mueller, P. Van Engen, and K. Buschow, New Class of Materials: Half-Metallic Ferromagnets, Phys. Rev. Lett. **50**, 2024 (1983).

[2] K. Ullakko, J. Huang, R. O'Handley, and V. Kokorin, Magnetically controlled shape memory effect in Ni_2MnGa intermetallics, Scr. Mater. **36**, 1133 (1997).

[3] J. Wernick, G. Hull, T. Geballe, J. Bernardini, and J. Waszczak, Superconductivity in ternary Heusler intermetallic compounds, Mater. Lett. **2**, 90 (1983).

[4] O. Meshcheriakova, S. Chadov, A. K. Nayak, U. K. Rößler, J. Kübler, G. André, A. A. Tsirlin, J. Kiss, S. Hausdorf, A. Kalache, W. Schnelle, M. Nicklas, and C. Felser, Large Noncollinearity and Spin Reorientation in the Novel Mn_2RhSn Heusler Magnet, Phys. Rev. Lett. **113**, 087203 (2014).

[5] T. Graf, C. Felser, and S. S. Parkin, Simple rules for the understanding of Heusler compounds, Prog. Solid State Chem. **39**, 1 (2011).

[6] S. Chadov, X. Qi, J. Kübler, G. H. Fecher, C. Felser, and S. C. Zhang, Tunable multifunctional topological insulators in ternary Heusler compounds, Nat. Mater. **9**, 541 (2010).

[7] P. Van Engen, K. Buschow, R. Jongebreur, and M. Erman, PtMnSb, a material with very high magneto-optical Kerr effect, Appl. Phys. Lett. **42**, 202 (1983).

[8] C. Uher, J. Yang, S. Hu, D. Morelli, and G. Meisner, Transport properties of pure and doped MNiSn (M = Zr, Hf), Phys. Rev. B **59**, 8615 (1999).

[9] S. Wolf, D. Awschalom, R. Buhrman, J. Daughton, S. Von Molnar, M. Roukes, A. Y. Chtchelkanova, and D. Treger, Spintronics: a spin-based electronics vision for the future, Science **294**, 1488 (2001).

[10] I. Galanakis and P. H. Dederichs, Half-metallicity and Slater-Pauling behavior in the ferromagnetic Heusler alloys, in *Half-metallic Alloys* (Springer-Verlag, Berlin, Heidelberg, 2005), pp. 1–39.

[11] M. Katsnelson, V. Y. Irkhin, L. Chioncel, A. Lichtenstein, and R. A. de Groot, Half-metallic ferromagnets: From band structure to many-body effects, Rev. Mod. Phys. **80**, 315 (2008).

[12] I. Galanakis, P. Dederichs, and N. Papanikolaou, Slater-Pauling behavior and origin of the half-metallicity of the full-Heusler alloys, Phys. Rev. B **66**, 174429 (2002).

[13] G. H. Fecher, H. C. Kandpal, S. Wurmehl, C. Felser, and G. Schönhense, Slater-Pauling rule and Curie temperature of Co_2-based Heusler compounds, J. Appl. Phys. **99**, 08J106 (2006).

[14] S. Wurmehl, G. H. Fecher, H. C. Kandpal, V. Ksenofontov, C. Felser, and H.-J. Lin, Investigation of Co_2FeSi: The Heusler compound with highest Curie temperature and magnetic moment, Appl. Phys. Lett. **88**, 032503 (2006).

[15] P. Brown, K.-U. Neumann, P. Webster, and K. Ziebeck, The magnetization distributions in some Heusler alloys proposed as half-metallic ferromagnets, J. Phys.: Condens. Matter **12**, 1827 (2000).

[16] T. Ishikawa, T. Marukame, H. Kijima, K.-I. Matsuda, T. Uemura, M. Arita, and M. Yamamoto, Spin-dependent tunneling characteristics of fully epitaxial magnetic tunneling junctions with a full-Heusler alloy Co_2MnSi thin film and a MgO tunnel barrier, Appl. Phys. Lett. **89**, 192505 (2006).

[17] Y. Sakuraba, K. Izumi, T. Iwase, S. Bosu, K. Saito, K. Takanashi, Y. Miura, K. Futatsukawa, K. Abe, and M. Shirai, Mechanism of large magnetoresistance in Co_2MnSi/Ag/Co_2MnSi devices with current perpendicular to the plane, Phys. Rev. B **82**, 094444 (2010).

[18] N. Tezuka, N. Ikeda, F. Mitsuhashi, and S. Sugimoto, Improved tunnel magnetoresistance of magnetic tunnel junctions with Heusler $Co_2FeAl_{0.5}Si_{0.5}$ electrodes fabricated by molecular beam epitaxy, Appl. Phys. Lett. **94**, 162504 (2009).

[19] B. C. S. Varaprasad, A. Srinivasan, Y. Takahashi, M. Hayashi, A. Rajanikanth, and K. Hono, Spin polarization and Gilbert damping of $Co_2Fe(Ga_xGe_{1-x})$ Heusler alloys, Acta Materialia **60**, 6257 (2012).

[20] C. Felser and A. Hirohata, *Heusler Alloys* (Springer International Publishing, Switzerland, 2015).

[21] K. R. Kumar, K. K. Bharathi, J. A. Chelvane, S. Venkatesh, G. Markandeyulu, and N. Harishkumar, First-principles calculation and experimental investigations on full-Heusler alloy Co_2FeGe, IEEE Trans. Mag. **45**, 3997 (2009).

[22] B. Venkateswarlu, P. Midhunlal, P. Babu, and N. H. Kumar, Magnetic and anomalous electronic transport properties of the quaternary Heusler alloys $Co_2Ti_{1-x}Fe_xGe$, J. Magn. Magn. Mater. **407**, 142 (2016).

[23] K. Srinivas, T. Prasanna Kumari, M. Manivel Raja, and S. Kamat, Effect of Fe substitution for Co on structure, electrical resistivity, and magnetic properties of Heusler type $Co_{2-x}Fe_{1+x}Si$ alloys, J. Appl. Phys. **114**, 033911 (2013).

[24] A. Köhler, L. Wollmann, D. Ebke, S. Chadov, C. Kaiser, Z. Diao, Y. Zheng, Q. Leng, and C. Felser, Tunable damping in the Heusler compound $Co_{2-x}Ir_xMnSi$, Phys. Rev. B **93**, 094410 (2016).

[25] I. Galanakis, P. Dederichs, and N. Papanikolaou, Origin and properties of the gap in the half-ferromagnetic Heusler alloys, Phys. Rev. B **66**, 134428 (2002).

[26] https://periodictable.com/Properties/A/AtomicRadius.an.pr.html

[27] See Supplemental Material at http://link.aps.org/supplemental/10.1103/PhysRevMaterials.3.114406 for further details in our experimental methods such that our results can be more easily reproduced.

[28] C. Boudias and D. Monceau, CaRine Crystallography: The Crystallographic Software for Research and Teaching.

[29] P. LeClair, X-ray Diffraction Calculation Software (2018).

[30] A. Putz and H. Brandenburg, Phase Identification from Power Diffraction, Crystal Impact Kreuzherrenstr. 102, 53227 Bonn, Germany.

[31] R. Datta, S. Kanuri, S. Karthik, D. Mazumdar, J. Ma, and A. Gupta, Formation of antiphase domains in $NiFe_2O_4$ thin films deposited on different substrates, Appl. Phys. Lett. **97**, 071907 (2010).

[32] L. Xiong, L. Yi, and G. Gao, Search for half-metallic magnets with large half-metallic gaps in the quaternary Heusler alloys CoFeTiZ and CoFeVZ (Z = Al, Ga, Si, Ge, As, Sb), J. Mag. Mag. Mater. **360**, 98 (2014).

[33] Y. Zhang, Z. Liu, G. Li, X. Ma, and G. Liu, Magnetism, band gap and stability of half-metallic property for the quaternary Heusler alloys CoFeTiZ (Z = Si, Ge, Sn), J. Alloys Comp. **616**, 449 (2014).

[34] J. B. Nelson and D. P. Riley, An experimental investigation of extrapolation methods in the derivation of accurate unit-cell dimensions of crystals, Proc. Phys. Soc. **57**, 160 (1945).

[35] M. Cohen, Precision lattice constants from X-ray powder photographs, Rev. Sci. Instruments **6**, 68 (1935).

[36] A. R. Denton and N. W. Ashcroft, Vegard's law, Phys. Rev. A **43**, 3161 (1991).

[37] B. Peters, A. Alfonsov, C. Blum, S. J. Hageman, P. Woodward, S. Wurmehl, B. Büchner, and F. Yang, Epitaxial films of Heusler compound $Co_2FeAl_{0.5}Si_{0.5}$ with high crystalline quality grown by off-axis sputtering, Appl. Phys. Lett. **103**, 162404 (2013).

[38] T. Marukame, T. Kasahara, K.-i. Matsuda, T. Uemura, and M. Yamamoto, Fabrication of fully epitaxial magnetic tunnel junctions using full-Heusler alloy $Co_2Cr_{0.6}Fe_{0.4}Al$ thin film and MgO tunnel barrier, Jpn. J. Appl. Phys. **44**, L521 (2005).

[39] M. Otto, R. Van Woerden, P. Van der Valk, J. Wijngaard, C. Van Bruggen, C. Haas, and K. Buschow, Half-metallic ferromagnets. I. Structure and magnetic properties of NiMnSb and related inter-metallic compounds, J. Phys.: Condens. Matter **1**, 2341 (1989).

[40] B. Deka, D. Chakraborty, and A. Srinivasan, Magnetic properties of $Co_2Fe(Ga_{1-x}Si_x)$ alloys, Physica B: Condens. Matter **448**, 173 (2014).

[41] V. Y. Irkhin and M. I. Katsnel'son, Half-metallic ferromagnets, Phys. Usp. **37**, 659 (1994).

[42] E. Wohlfarth, Magnetic properties of crystalline and amorphous alloys: A systematic discussion based on the Rhodes-Wohlfarth plot, J. Magn. Magn. Mater. **7**, 113 (1978).

[43] L. Pal, S. Gupta, K. Suresh, and A. Nigam, Effect of Cr substitution on the magnetic and magnetic-transport properties of $Fe_2Mn_{1-x}Cr_xSi$ alloys, J. Appl. Phys. **115**, 17C303 (2014).

[44] N. Dung, L. Zhang, Z. Ou, L. Zhao, L. Van Eijck, A. Mulders, M. Avdeev, E. Suard, N. Van Dijk, and E. Brück, High/low-moment phase transition in hexagonal Mn-Fe-P-Si compounds, Phys. Rev. B **86**, 045134 (2012).

[45] M. Getzlaff, *Fundamentals of Magnetism* (Springer-Verlag, Berlin, Heidelberg, 2007).

[46] W. Marshall and S. W. Lovesey, Theory of thermal neutron scattering: the use of neutrons for the investigation of condensed matter, Science **177**, 50 (1971).

[47] R. Y. Umetsu, A. Okubo, A. Fujita, T. Kanomata, K. Ishida, and R. Kainuma, Spin Wave-Stiffness Constants of Half-Metallic Ferromagnets Co_2YZ (Y = Cr, Mn, and Fe, Z = Ga, Al, and Si) Heusler alloys, IEEE Trans. Magn. **47**, 2451 (2011).

[48] S. Trudel, O. Gaier, J. Hamrle, and B. Hillebrands, Magnetic anisotropy, exchange and damping in cobalt-based full-Heusler compounds: An experimental review, J. Phys. D **43**, 193001 (2010).

[49] L. Ritchie, G. Xiao, Y. Ji, T. Chen, C. Chien, M. Zhang, J. Chen, Z. Liu, G. Wu, and X. Zhang, Magnetic, structural, and transport properties of the Heusler alloys Co_2MnSi and NiMnSb, Phys. Rev. B **68**, 104430 (2003).

[50] F. Bolzoni and R. Cabassi, Review of singular point detection techniques, Physica B: Condens. Matter **346**, 524 (2004).

[51] L. van der Pauw, A method of measuring specific resistivity and Hall effect of discs of arbitrary shape, Philips Res. Rep **13**, 1 (1958).

[52] P. L. Rossiter, *The Electrical Resistivity of Metals and Alloys* (Cambridge University Press, Cambridge, 1991), Vol. 6.

[53] J. S. Moodera and D. M. Mootoo, Nature of half-metallic ferromagnets: Transport studies, J. Appl. Phys. **76**, 6101 (1994).

[54] A. Barry, J. Coey, L. Ranno, and K. Ounadjela, Evidence for a gap in the excitation spectrum of CrO_2, J. Appl. Phys. **83**, 7166 (1998).

[55] D. Bombor, C. G. Blum, O. Volkonskiy, S. Rodan, S. Wurmehl, C. Hess, and B. Büchner, Half-Metallic Ferromagnetism with Unexpectedly Small Spin Splitting in the Heusler Compound Co_2FeSi, Phys. Rev. Lett. **110**, 066601 (2013).

[56] G. Rogl, A. Grytsiv, M. Gürth, A. Tavassoli, C. Ebner, A. Wünschek, S. Puchegger, V. Soprunyuk, W. Schranz, E. Bauer *et al.*, Mechanical properties of half-Heusler alloys, Acta Mater. **107**, 178 (2016).

[57] M. Hakimi, P. Kameli, H. Salamati, and Y. Mazaheri, Evolution of microstructural and mechanical properties of nanocrystalline Co_2FeAl Heusler alloy prepared by mechanical alloying, Powder Metall. **56**, 111 (2013).

[58] S. Ouardi, G. H. Fecher, B. Balke, A. Beleanu, X. Kozina, G. Stryganyuk, C. Felser, W. Klöß, H. Schrader, F. Bernardi *et al.*, Electronic and crystallographic structure, hard x-ray photoemission, and mechanical and transport properties of the half-metallic Heusler compound Co_2MnGe, Phys. Rev. B **84**, 155122 (2011).

[59] L. Zhang, G. Rogl, A. Grytsiv, S. Puchegger, J. Koppensteiner, F. Spieckermann, H. Kabelka, M. Reinecker, P. Rogl, W. Schranz *et al.*, Mechanical properties of filled antimonide skutterudites, Mater. Sci. Eng. B **170**, 26 (2010).

[60] G. Kresse and J. Furthmüller, Efficiency of ab-initio total energy calculations for metals and semiconductors using a plane-wave basis set, Comput. Mater. Sci. **6**, 15 (1996).

[61] P. E. Blöchl, Projector augmented-wave method, Phys. Rev. B **50**, 17953 (1994).

[62] J. P. Perdew, K. Burke, and M. Ernzerhof, Generalized Gradient Approximation Made Simple, Phys. Rev. Lett. **77**, 3865 (1996).

[63] J. Ma, J. He, D. Mazumdar, K. Munira, S. Keshavarz, T. Lovorn, C. Wolverton, A. W. Ghosh, and W. H. Butler, Computational investigation of inverse Heusler compounds for spintronics applications, Phys. Rev. B **98**, 094410 (2018).

[64] G. Bergerhoff and I. D. Brown, in *Crystallographic Databases*, edited by F. H. Allen, G. Bergerhoff, and R. Sievers (International Union of Crystallography, Chester, UK, 1987), Vol. 360, p. 77.

[65] A. Belsky, M. Hellenbrandt, V. L. Karen, and P. Luksch, New developments in the Inorganic Crystal Structure Database (ICSD): accessibility in support of materials research and design, Acta Crystallogr., Sect. B: Struct. Sci. **58**, 364 (2002).

[66] J. E. Saal, S. Kirklin, M. Aykol, B. Meredig, and C. Wolverton, Materials design and discovery with high-throughput density functional theory: the open quantum materials database (OQMD), JOM **65**, 1501 (2013).

[67] S. Kirklin, J. E. Saal, B. Meredig, A. Thompson, J. W. Doak, M. Aykol, S. Rühl, and C. Wolverton, The Open Quantum Materials Database (OQMD): assessing the accuracy of DFT formation energies, npj Comp. Mater. **1**, 15010 (2015).

[68] W. H. Butler, A. W. Gosh *et al.*, Heuslers home, http://heusleralloys.mint.ua.edu

[69] W. H. Butler, C. K. Mewes, C. Liu, and T. Xu, Rational design of half-metallic heterostructures, arXiv:1103.3855 [cond-mat.mtrl-sci].